FINITE-VOLUME WENO SCHEMES FOR THREE-DIMENSIONAL CONSERVATION LAWS

V.A. Titarev[1] and E.F. Toro[2]

[1] Department of Mathematics, Faculty of Science,
University of Trento, Trento, Italy,
E-mail: titarev@science.unitn.it,
Web page: http://www.science.unitn.it/∼titarev

[2] Laboratory of Applied Mathematics, Faculty of Engineering,
University of Trento, Trento, Italy,
E-mail: toro@ing.unitn.it,
Web page: http://www.ing.unitn.it/toro

Abstract

The purpose of this paper is twofold. Firstly we carry out an extension of the finite-volume WENO approach to three space dimensions and higher orders of spatial accuracy (up to eleventh order). Secondly, we propose to use three new fluxes as a building block in WENO schemes. These are the one-stage HLLC [29] and FORCE [24] fluxes and a recent multi-stage MUSTA flux [26]. The numerical results in one, two and three space dimensions suggest the the new centred WENO-FORCE and upwind WENO-HLLC and WENO-MUSTA schemes achieve a uniformly high order of accuracy for smooth solutions and produce essentially non-oscillatory profiles for discontinuities. In particular, the WENO-MUSTA scheme combines the simplicity of the centred non-staggered WENO-FORCE scheme and accuracy of the upwind WENO-HLLC scheme with a complete Riemann solver. The advantages of the WENO-MUSTA scheme will be fully realised when solving very complex hyperbolic systems, such as those arising in multi-phase flows, magnetohydrodynamics and general relativity.

Key words: high-order schemes, weighted essentially non-oscillatory, HLLC flux, FORCE flux, MUSTA flux, two and three space dimensions.

1 Introduction

Finite-volume weighted essentially non-oscillatory (WENO) schemes [15, 10, 19, 6, 13, 14, 16] represent the state-of-the art in numerical methods for hyperbolic conservation laws in one and two space dimensions. Though more expensive than the corresponding finite-difference WENO schemes [7, 1], they can be applied not only on structured Cartesian meshes but also on more general unstructured meshes, e.g. [10, 19]. Upwind WENO schemes [15, 10, 19, 6, 16] use wave propagation information explicitly in the building block of the scheme, which is obtained by performing a local characteristic decomposition of the physical flux and using the Rusanov first-order upwind flux [18] for each characteristic field. The present centred WENO schemes, see e.g. [13, 14, 16] and references therein, utilize the staggered-mesh framework and do not use wave propagation information explicitly.

The motivation of this paper is to develop improved finite-volume WENO schemes. The improvements are twofold. Firstly, we generalize the existing non-staggered two-dimensional schemes [19, 6] to three space dimensions and use polynomial reconstructions of higher order. We consider schemes of up to 11^{th} order of spatial accuracy. In multiple space dimensions the flux computation in these schemes involves the use of a high-order Gaussian quadrature for integration over cell sides in two space dimensions and cell faces in three space dimensions. Consequently, WENO reconstructed values are needed for each Gaussian integration point. We provide the precise information on the reconstruction weights and values for these points so that the schemes can be easily coded.

Secondly, we propose to use three new fluxes as the building block in WENO schemes. The first flux is the HLLC flux [29], which is an improved variant of the HLL flux [9] in that it contains the middle (contact) wave in the Riemann problem solution. The HLLC flux does not use linearizations of the equations and works well for low-density problems and sonic points without any fixes. The use of this flux in the WENO framework gives a new upwind WENO-HLLC scheme.

The second flux which we propose to use is the flux of the **F**irst-**O**rder **C**entred scheme (FORCE) [24, 25]. Compared to the well-known centred Lax-Friedrichs flux, the FORCE flux has smaller numerical viscosity (by a factor of two) and does not produce undesirable coupling of cells when used in a first order scheme. To our knowledge, the new WENO-FORCE scheme is the first non-staggered mesh centred WENO scheme.

The last flux we propose to use in the design of the WENO schemes is a recent upwind **M**ulti-**S**tage (MUSTA) flux [26]. The MUSTA family of fluxes achieves upwinding by solving the local Riemann problem at the cell interface numerically, rather than analytically, and thus does not need any information on the details of Riemann problem solution. The four-stage MUSTA flux essentially matches the accuracy of the most accurate Riemann solvers, such as the exact Riemann solver [5], Roe Riemann solver [17] with an entropy fix or HLLC Riemann solver [29, 25]. The new WENO-MUSTA scheme therefore combines the good accuracy of the best upwind schemes and the simplicity of centred schemes. Some researches would refer to this scheme as the *Riemann-solver-free* upwind scheme.

The rest of the paper is organised as follows. In Section 2 we describe the general semi-discrete WENO framework in three space dimensions. In Section 3 we give all details on the reconstruction procedure in three space dimensions. The FORCE, HLLC and MUSTA fluxes are reviewed in Section 4. Numerical results of the new WENO-FORCE, WENO-HLLC and

WENO-MUSTA schemes in one, two and three space dimensions are presented in Section 5. Conclusions are drawn in Section 6.

2 General framework in three space dimensions

Consider three-dimensional hyperbolic systems in conservation form

$$\partial_t \mathbf{Q} + \partial_x \mathbf{F}(\mathbf{Q}) + \partial_y \mathbf{G}(\mathbf{Q}) + \partial_z \mathbf{H}(\mathbf{Q}) = \mathbf{0}, \tag{1}$$

where $\mathbf{Q}(x, y, z, t)$ is the vector of unknown conservative variables and $\mathbf{F}(\mathbf{Q})$, $\mathbf{G}(\mathbf{Q})$ and $\mathbf{H}(\mathbf{Q})$ are physical flux vectors in x, y and z coordinate directions respectively. The semi-discrete finite volume methods begin by considering a control volume (a computation cell) I_{ijk} in $x - y - z$ space

$$I_{ijk} = \left[x_{i-\frac{1}{2}}, x_{i+\frac{1}{2}}\right] \times \left[y_{j-\frac{1}{2}}, y_{j+\frac{1}{2}}\right] \times \left[z_{k-\frac{1}{2}}, z_{k+\frac{1}{2}}\right], \tag{2}$$

with the dimensions given by

$$\Delta x = x_{i+\frac{1}{2}} - x_{i-\frac{1}{2}}\ ,\ \Delta y = y_{j+\frac{1}{2}} - y_{j-\frac{1}{2}}\ ,\ \Delta z = z_{k+\frac{1}{2}} - z_{k-\frac{1}{2}}. \tag{3}$$

Integrating (1) over the control volume I_{ijk}, we obtain the following semi-discrete relations

$$\begin{aligned} \frac{d}{dt}\mathbf{Q}_{ijk}(t) = \ & \frac{1}{\Delta x}\left(\mathbf{F}_{i-1/2,jk} - \mathbf{F}_{i+1/2,jk}\right) + \frac{1}{\Delta y}\left(\mathbf{G}_{i,j-1/2,k} - \mathbf{G}_{i,j+1/2,k}\right) + \\ & \frac{1}{\Delta z}\left(\mathbf{H}_{ij,k-1/2} - \mathbf{H}_{ij,k+1/2}\right), \end{aligned} \tag{4}$$

where $\mathbf{Q}_{ijk}(t)$ is the space average of the solution in cell I_{ijk} at time t

$$\mathbf{Q}_{ijk}(t) = \frac{1}{\Delta x}\frac{1}{\Delta y}\frac{1}{\Delta z}\int_{x_{i-1/2}}^{x_{i+1/2}}\int_{y_{j-1/2}}^{y_{j+1/2}}\int_{z_{k-1/2}}^{z_{k+1/2}} \mathbf{Q}(x, y, z, t)\, dzdydx \tag{5}$$

and $\mathbf{F}_{i+1/2,jk}$, $\mathbf{G}_{i,j+1/2,k}$ and $\mathbf{H}_{ij,k+1/2}$ are space averages of physical fluxes over cell faces at time t:

$$\begin{aligned} \mathbf{F}_{i+1/2,jk} &= \frac{1}{\Delta y}\frac{1}{\Delta z}\int_{y_{j-1/2}}^{y_{j+1/2}}\int_{z_{k-1/2}}^{z_{k+1/2}} \mathbf{F}(\mathbf{Q}(x_{i+1/2}, y, z, t))\, dzdy, \\ \mathbf{G}_{i,j+1/2,k} &= \frac{1}{\Delta x}\frac{1}{\Delta z}\int_{x_{i-1/2}}^{x_{i+1/2}}\int_{z_{k-1/2}}^{z_{k+1/2}} \mathbf{G}(\mathbf{Q}(x, y_{j+1/2}, z, t))\, dzdx, \\ \mathbf{H}_{ij,k+1/2} &= \frac{1}{\Delta x}\frac{1}{\Delta y}\int_{x_{i-1/2}}^{x_{i+1/2}}\int_{y_{j-1/2}}^{y_{j+1/2}} \mathbf{H}(\mathbf{Q}(x, y, z_{k+1/2}, t))\, dydx. \end{aligned} \tag{6}$$

Expressions (5), (6) so far are exact relations, but can also be used in the construction of high-order accurate semi-discrete schemes if $\mathbf{Q}_{ijk}(t)$, $\mathbf{F}_{i+1/2,jk}$, $\mathbf{G}_{i,j+1/2,k}$ and $\mathbf{H}_{ij,k+1/2}$ are regarded as numerical approximations to the corresponding exact quantities. Let us denote these approximations by the same symbols as the exact values in (5), (6). The simplest scheme which can be considered from the above framework results from assuming initial data at time t^n as given by a set of piece-wise constant values $\mathbf{Q}_{ijk}$ and using the Euler time-stepping to discretize the time derivative. Godunov [5] first proposed to use the Riemann problem solution for the computation of numerical fluxes resulting in his famous first-order conservative upwind scheme. A popular approach to the construction of second order Godunov methods,

pioneered by Kolgan [11, 12] and developed further by van Leer [31], relies on piece-wise linear reconstruction of data inside each computational cell. Finally, finite-volume essentially non-oscillatory schemes [8, 2, 10, 19] can be regarded as uniformly high order extensions of this approach in two space dimensions in which data is represented by polynomials of arbitrary order and TVD Runge-Kutta methods are used for the discretization of the ODE system (4).

The procedure to evaluate numerical fluxes (6) in three space dimensions is a straightforward extension of the corresponding two-dimensional one [2, 10, 19, 6] and consists of three main steps. The first step is to discretize the integrals over the faces (6) using a suitable Gaussian numerical quadrature. For the rest of the paper we shall concentrate on $\mathbf{F}_{i+1/2,jk}$; the expressions for $\mathbf{G}_{i,j+1/2,k}$ and $\mathbf{H}_{ij,k+1/2}$ are obtained in an entirely analogous manner. The application of the tensor product of a one-dimensional N-point quadrature rule to (6) yields the following expression for the flux in the x coordinate direction:

$$\mathbf{F}_{i+1/2,j,k} = \frac{1}{\Delta y}\frac{1}{\Delta z}\sum_{\alpha=1}^{N}\sum_{\beta=1}^{N}\mathbf{F}(\mathbf{Q}(x_{i+1/2}, y_\alpha, z_\beta))K_\beta K_\alpha, \tag{7}$$

where the subscripts α, β correspond to different Gaussian integration points y_α, z_β and weights K_α, K_β. Expression (7) involves point-wise values of $\mathbf{Q}$ whereas the scheme evolves the cell averages of $\mathbf{Q}$. Thus the second step in evaluating the fluxes is to reconstruct the point-wise values of the solution from cell averages and obtain high-order accurate approximations to the values of $\mathbf{Q}$ at the integration points. In WENO schemes this is achieved by means of weighted essentially non-oscillatory (WENO) adaptive-stencil reconstruction procedure [15, 7], which estimates the smoothness of the solution and constructs the reconstruction polynomial in such a way so as to avoid interpolation across discontinuities. After the reconstruction is carried out at each face we have two sets of values of $\mathbf{Q}$, corresponding to $x_{i+1/2} - 0$ and $x_{i+1/2} + 0$ which are often called left and right boundary extrapolated values:

$$\begin{aligned}
\mathbf{Q}^L_{i+1/2,\alpha,\beta} &= \mathbf{Q}(x_{i+1/2} - 0, y_\alpha, z_\beta),\\
\mathbf{Q}^R_{i+1/2,\alpha,\beta} &= \mathbf{Q}(x_{i+1/2} + 0, y_\alpha, z_\beta),\\
\alpha, \beta &= 1, \ldots N.
\end{aligned} \tag{8}$$

The last step in the evaluation of the fluxes is to replace $\mathbf{F}(\mathbf{Q}(x_{i+1/2}, y_\alpha, z_\beta))$ in (7) by a certain monotone function of left and right boundary extrapolated values $\hat{\mathbf{F}}(\mathbf{Q}^L, \mathbf{Q}^R)$, the building block of the WENO scheme, or numerical flux:

$$\mathbf{F}_{i+1/2,j,k} = \frac{1}{\Delta y}\frac{1}{\Delta z}\sum_{\alpha=1}^{N}\sum_{\beta=1}^{N}\hat{\mathbf{F}}(\mathbf{Q}^L_{i+1/2,\alpha,\beta}, \mathbf{Q}^R_{i+1/2,\alpha,\beta})K_\beta K_\alpha. \tag{9}$$

To retain uniformly high order of time accuracy the solution is advanced in time by means of TVD Runge-Kutta methods. Usually, the following third order three-stage method [20] is used:

$$\begin{aligned}
\mathbf{Q}^{(1)}_{ijk} &= \mathbf{Q}^n_{ijk} + \Delta t\, \mathbf{L}_{ijk}(\mathbf{Q}^n),\\
\mathbf{Q}^{(2)}_{ijk} &= \frac{3}{4}\mathbf{Q}^n_{ijk} + \frac{1}{4}\mathbf{Q}^{(1)}_{ijk} + \frac{1}{4}\Delta t\, \mathbf{L}_{ijk}(\mathbf{Q}^{(1)}),\\
\mathbf{Q}^{n+1}_{ijk} &= \frac{1}{3}\mathbf{Q}^n_{ijk} + \frac{2}{3}\mathbf{Q}^{(2)}_{ijk} + \frac{2}{3}\Delta t\, \mathbf{L}_{ijk}(\mathbf{Q}^{(2)}),
\end{aligned} \tag{10}$$

where $\mathbf{L}_{ijk}(\mathbf{Q})$ denotes the spatial operator (right hand side of (4)) at the appropriate time level. The above procedure of flux evaluation must be carried out during each stage of the Runge-Kutta method. Another, more recent, forth order *five-stage* Runge-Kutta method can be found in [21]; see the original paper for details.

The explicit scheme considered above requires the computation of a time step Δt to be used in (10), such that stability of the numerical method is ensured. One way of choosing Δt is

$$\Delta t = C_{cfl} \times \min_{ijk} \left(\frac{\Delta x}{|S_{ijk}^{n,x}|}, \frac{\Delta y}{|S_{ijk}^{n,y}|}, \frac{\Delta z}{|S_{ijk}^{n,z}|} \right). \tag{11}$$

Here $S_{ijk}^{n,d}$ is the speed of the fastest wave present at time level n travelling in the d direction, with $d = x, y, z$. C_{cfl} is the CFL number and is chosen according to the linear stability condition of the scheme. When the three-stage Runge-Kutta method (10) is used in one space dimension the WENO schemes have the optimal stability condition of Courant number

$$0 < C_{cfl} \leq 1. \tag{12}$$

The two-dimensional and three dimensional schemes have the reduced stability conditions, which in fact coincide with those of the unsplit Godunov scheme in two and three space dimensions. In two space dimensions the stability condition is

$$0 < C_{cfl} \leq 1/2. \tag{13}$$

Our numerical experiments show that in three space dimensions the stability condition is

$$0 < C_{cfl} \leq 1/3. \tag{14}$$

For the forth order Runge-Kutta method of [21] the time step can be increased by 50% so that stability conditions (12) - (14) become $0 < C_{cfl} \leq 3/2$, $0 < C_{cfl} \leq 3/4$ and $0 < C_{cfl} \leq 1/2$ respectively. We remark that the error of the forth order Runge-Kutta method grows very fast when the CFL number exceeds the conventional values (12) - (14), see the original paper [21] for details. Therefore, we still use (12) - (14) for choosing the time step.

The description of the scheme is complete when an algorithm to calculate the values of $\mathbf{Q}$ at Gaussian integration points is given and a flux function $\hat{\mathbf{F}}(\mathbf{Q}^L, \mathbf{Q}^R)$ is chosen. In the following sections we give details on the WENO reconstruction and the numerical flux. It is sufficient to explain the general three-dimensional case; the two and one dimensional cases will follow easily.

3 WENO reconstruction in three space dimensions

3.1 Scalar finite-volume reconstruction

The reconstruction problem we face is the following. Given spatial averages of a scalar function $q(x, y, z)$ in a cell I_{ijk}

$$q_{ijk} = \frac{1}{\Delta x}\frac{1}{\Delta y}\frac{1}{\Delta z}\int_{x_{i-1/2}}^{x_{i+1/2}}\int_{y_{j-1/2}}^{y_{j+1/2}}\int_{z_{k-1/2}}^{z_{k+1/2}} q(x, y, z)\, dz\, dy\, dx, \tag{15}$$

we want to compute the point-wise value of q at Gaussian integration points $(x_{i+1/2}, y_\alpha, z_\beta)$ so that the reconstruction procedure is conservative and these reconstructed values are of high-order of accuracy. There are essentially two ways of accomplishing this: genuine multidimensional reconstruction and dimension-by-dimension reconstruction. The genuine multidimensional reconstruction [10, 19] considers all cells in the multidimensional stencil simultaneously to build up a reconstruction polynomial, whereas dimension-by-dimension reconstruction [2, 19] consists of a number of one-dimensional reconstruction sweeps. The dim-by-dimdimension-by-dimension reconstruction is much simpler and less computationally expensive than the genuine multidimensional one; this is especially so in three space dimensions. Therefore, in this paper we use the dimension-by-dimension reconstruction throughout.

The general idea of dimension-by-dimension reconstruction in two space dimensions is explained in [2] in the context of the ENO schemes. The extension to three space dimensions is straightforward and consists of three steps. Recall that we need left $q^L_{i+1/2,\alpha\beta}$ and right $q^R_{i+1/2,\alpha\beta}$ extrapolated values. For the left values the stencil consists of cells $I_{i_x i_y i_z}$ such that

$$i - r \le i_x \le i + r, \quad j - r \le i_y \le j + r, \quad k - r \le i_z \le k + r, \tag{16}$$

where $r - 1$ is the order of polynomials used in WENO sweeps, e.g. $r = 3$ corresponds to the weighted piece-wise parabolic reconstruction and so on. For the right values the stencil consists of cells for which $i + 1 - r \le i_x \le i + 1 + r$ and i_y, i_z vary according to (16).

In the first step of the three-dimensional reconstruction for all indexes i_y, i_z from the stencil we perform the one-dimensional WENO reconstruction in the x coordinate direction (normal to the cell face) and obtain two-dimensional averages with respect to $y - z$ coordinate directions:

$$\begin{aligned} v^L_{i_y i_z} &= \frac{1}{\Delta y}\frac{1}{\Delta z}\int_{y_{i_y-1/2}}^{y_{i_y+1/2}}\int_{z_{i_z-1/2}}^{z_{i_z+1/2}} q(x_{i+1/2} - 0, y, z)\, dz\, dy, \\ v^R_{i_y i_z} &= \frac{1}{\Delta y}\frac{1}{\Delta z}\int_{y_{i_y-1/2}}^{y_{i_y+1/2}}\int_{z_{i_z-1/2}}^{z_{i_z+1/2}} q(x_{i+1/2} + 0, y, z)\, dz\, dy. \end{aligned} \tag{17}$$

In the second step we perform one-dimensional reconstruction in y coordinate direction for all values of i_z and obtain one-dimensional averages of the solution with respect to z coordinate direction

$$\begin{aligned} w^L_{i_z} &= \frac{1}{\Delta z}\int_{z_{i_z-1/2}}^{z_{i_z+1/2}} q(x_{i+1/2} - 0, y_\alpha, z)\, dz, \\ w^R_{i_z} &= \frac{1}{\Delta z}\int_{z_{i_z-1/2}}^{z_{i_z+1/2}} q(x_{i+1/2} + 0, y_\alpha, z)\, dz \end{aligned} \tag{18}$$

in lines corresponding to the Gaussian integration points on the y axis ($x = x_{i+1/2}$, $y = y_\alpha$). Finally, for each line ($x = x_{i+1/2}$, $y = y_\alpha$) we obtain reconstructed point-wise values $q(x_{i+1/2}, y_\alpha, z_\beta)$ by again applying the one-dimensional reconstruction now to $w^L_{i_z}$, $w^R_{i_z}$ in the z coordinate direction. We note that it is also possible to do the z sweep in the second step instead of y sweep.

The two-dimensional reconstruction is obtained by using only two first steps in the above algorithm.

We now proceed to define the reconstructed values for each of the one-dimensional WENO sweeps. We do so in terms of reconstructions of one-dimensional averages u_i of a function $u(\xi)$

$$u_i = \frac{1}{\Delta\xi}\int_{\xi_{i-1/2}}^{\xi_{i+1/2}} u(\xi)\, d\xi, \tag{19}$$

where $\Delta\xi$ is the cell size: $\Delta\xi = \xi_{i+1/2} - \xi_{i-1/2}$. Recall that in one space dimension for any order of accuracy r there are r candidate stencils for reconstruction. For each such stencil of r cells there is a corresponding $(r-1)^{th}$-order polynomial $p_l(\xi)$, $l = 0, \dots r-1$. The WENO reconstruction procedure [15, 7] defines the reconstructed value as a convex combination of r^{th}-order accurate values of all polynomials, taken with positive non-linear weights. The weights are chosen in such a way as to mimic the ENO idea [8, 2] when the solution is not sufficiently smooth and achieve $(2r-1)^{th}$ order of accuracy when it is smooth. For a given point $\tilde{\xi}$ the design of weights consists of three steps. First, one finds the so-called optimal weights d_l so that the combination of all polynomials with this weights produces the value of the polynomial of order $(2r-1)$ corresponding to the large stencil. Next, if optimal weights d_l are all positive one defines the non-linear weights ω_l as

$$\alpha_l = \frac{d_l}{(10^{-6} + \beta_l)^2}, \quad \omega_l = \frac{\alpha_k}{\sum_{l=0}^{r-1} \alpha_l}, \quad l = 0, \dots r-1. \tag{20}$$

Here β_l are the so-called smoothness indicators [7]:

$$\beta_l = \sum_{m=1}^{r-1} \int_{\xi_{i-1/2}}^{\xi_{i+1/2}} \left(\frac{d^m}{dx^m} p_l(\xi) \right)^2 \Delta\xi^{2m-1} d\xi, \quad l = 0, \dots r-1. \tag{21}$$

If some of d_l are negative then a special procedure to handle such negative weights must be used, see [19] for details. The final WENO reconstructed value is then given by

$$u(\tilde{\xi}) = \sum_{l=0}^{r-1} p_l(\tilde{\xi}) w_l. \tag{22}$$

In several space dimensions the one-dimensional WENO procedure is applied during each one-dimensional sweep. For the first sweep (normal to the cell face) the weights are designed to obtain reconstructed values at $x_{i+1/2}$; the corresponding linear weights d_l and smoothness indicators β_l can be found in [7, 1] for $r = 2 \dots, 6$. For the second and third steps the weights, which will be different from the first step, are designed to achieve high accuracy for Gaussian integration points y_α, z_β. The values of the weights are tailored to a specific Gaussian integration rule used to discretize space integrals (7), (9). Our numerical experiments show that the best results in terms of accuracy and computational cost for $r = 3, 4$ are obtained if the the following two-point (forth order) Gaussian quadrature is used:

$$\int_{-1}^{1} \varphi(\xi)\, d\xi = \varphi\left(-\frac{1}{\sqrt{3}}\right) + \varphi\left(+\frac{1}{\sqrt{3}}\right). \tag{23}$$

even though the use of (23) leads to formal forth order spatial accuracy. For schemes with higher order reconstructions ($r = 5$ and $r = 6$) we have tested different quadratures corresponding to $N = 2, 3, 4$ and found that the most accurate results are obtained when the four-point quadrature is used. The two-point rule (23), however, still works well.

The WENO sweep in the x coordinate direction (normal to the cell face) corresponds to the left and right reconstructed values at $\xi_{i+1/2}$ whereas the y and z sweeps need values at the Gaussian points ξ_α; for the two-point quadrature (23) these are $\xi_i \pm \Delta\xi/(2\sqrt{3})$. It appears that the weights and reconstruction formulas for the Gaussian integration points ξ_α have not been reported in the literature so far. Therefore, in order to provide the complete information about the scheme below we give all necessary information for one dimensional sweeps in the fifth order ($r = 3$) and seventh order ($r = 4$) WENO reconstructions. Higher order piece-wise quadric ($r = 5$) and quintic ($r = 6$) reconstructions are omitted.

3.2 Piece-wise parabolic WENO reconstruction ($r = 3$)

We consider a cell $[\xi_{i-1/2}, \xi_{i+1/2}]$ and provide expressions for $u(\xi_{i+1/2} - 0)$, $u(\xi_{i-1/2} + 0)$ and $u(\xi_i \pm \Delta\xi/(2\sqrt{3}))$. The three candidate stencils for reconstruction are

$$S_0 = (i, i+1, i+2), \quad S_1 = (i-1, i, i+1), \quad S_2 = (i-2, i-1, i). \tag{24}$$

The corresponding smoothness indicators are given by [7]

$$\begin{aligned}
\beta_0 &= \frac{13}{12}(u_i - 2u_{i+1} + u_{i+2})^2 + \frac{1}{4}(3u_i - 4u_{i+1} + u_{i+2})^2, \\
\beta_1 &= \frac{13}{12}(u_{i-1} - 2u_i + u_{i+1})^2 + \frac{1}{4}(u_{i-1} - u_{i+1})^2, \\
\beta_2 &= \frac{13}{12}(u_{i-2} - 2u_{i-1} + u_i)^2 + \frac{1}{4}(u_{i-2} - 4u_{i-1} + 3u_i)^2.
\end{aligned} \tag{25}$$

The optimal weights d_l for the left extrapolated value $u^L_{i+1/2}$ at $x_{i+1/2}$ are given by [7]:

$$d_0 = \frac{3}{10}, \quad d_1 = \frac{3}{5}, \quad d_2 = \frac{1}{10} \tag{26}$$

and $u^L_{i+1/2}$ is given by

$$\begin{aligned}
u^L_{i+1/2} = u(\xi_{i+1/2} - 0) = \frac{1}{6}\omega_0(-u_{i+2} + 5u_{i+1} + 2u_i) + \\
\frac{1}{6}\omega_1(-u_{i-1} + 5u_i + 2u_{i+1}) + \frac{1}{6}\omega_2(2u_{i-2} - 7u_{i-1} + 11u_i).
\end{aligned} \tag{27}$$

The optimal weights d_l for right boundary extrapolated value $u^R_{i-1/2}$ at $x_{i-1/2}$ are obtained by symmetry

$$d_0 = \frac{1}{10}, \quad d_1 = \frac{3}{5}, \quad d_2 = \frac{3}{10} \tag{28}$$

and $u^R_{i-1/2}$ is given by

$$\begin{aligned}
u^R_{i-1/2} = u(\xi_{i-1/2} + 0) = \frac{1}{6}\omega_0(2u_{i+2} - 7u_{i+1} + 11u_i) + \\
\frac{1}{6}\omega_1(-u_{i+1} + 5u_i + 2u_{i-1}) + \frac{1}{6}\omega_2(-u_{i-2} + 5u_{i-1} + 2u_i).
\end{aligned} \tag{29}$$

For the first Gaussian integration point $\xi = \xi_i - \Delta\xi/(2\sqrt{3})$ the optimal weights are as follows:

$$d_0 = \frac{210 - \sqrt{3}}{1080}, \quad d_1 = \frac{11}{18}, \quad d_2 = \frac{210 + \sqrt{3}}{1080} \tag{30}$$

and the reconstructed value is given by

$$\begin{aligned}
u\left(\xi_i - \frac{\Delta\xi}{2\sqrt{3}}\right) = \omega_0\left[u_i + (3u_i - 4u_{i+1} + u_{i+2})\frac{\sqrt{3}}{12}\right] + \\
\omega_1\left[u_i - (-u_{i-1} + u_{i+1})\frac{\sqrt{3}}{12}\right] + \omega_2\left[u_i - (3u_i - 4u_{i-1} + u_{i-2})\frac{\sqrt{3}}{12}\right].
\end{aligned} \tag{31}$$

For the second Gaussian integration point $\xi = \xi_i + \Delta\xi/(2\sqrt{3})$ the optimal weights are obtained from symmetry by interchanging d_0 and d_2 in (30)

$$d_0 = \frac{210+\sqrt{3}}{1080}, \quad d_1 = \frac{11}{18}, \quad d_2 = \frac{210-\sqrt{3}}{1080}. \tag{32}$$

The reconstructed value is

$$\begin{aligned} u\left(\xi_i + \frac{\Delta\xi}{2\sqrt{3}}\right) = \omega_0 \left[u_i - (3u_i - 4u_{i+1} + u_{i+2})\frac{\sqrt{3}}{12}\right] + \\ \omega_1 \left[u_i - (u_{i-1} - u_{i+1})\frac{\sqrt{3}}{12}\right] + \omega_2 \left[u_i - (-3u_i + 4u_{i-1} - v_{i-2})\frac{\sqrt{3}}{12}\right]. \end{aligned} \tag{33}$$

We note that the nonlinear weights ω_l must be computed according to (20) *separately* for each of the points $\xi_i \pm \Delta\xi/(2\sqrt{3})$.

3.3 Piece-wise cubic WENO reconstruction ($r = 4$)

The four candidate stencils are

$$\begin{aligned} S_0 = (i, i+1, i+2, i+3), \quad S_1 = (i-1, i, i+1, i+2), \\ S_2 = (i-2, i-1, i, i+1), \quad S_3 = (i-3, i-2, i-1, i). \end{aligned} \tag{34}$$

The corresponding smoothness indicators are given by [1]

$$\begin{aligned} \beta_0 &= 2107u_i^2 - 9402u_{i+1}u_i + 7042u_iu_{i+2} - 1854u_iu_{i+3} - 17246u_{i+1}u_{i+2} \\ &\quad -3882u_{i+2}u_{i+3} + 11003u_{i+1}^2 + 7043u_{i+2}^2 + 547u_{i+3}^2 + 4642u_{i+1}u_{i+3}, \\ \beta_1 &= 267u_{i+2}^2 - 1642u_{i+2}u_{i+1} + 1602u_{i+2}u_i - 494u_{i+2}u_{i-1} - 2522u_iu_{i-1} + 3443u_i^2 \\ &\quad +547u_{i-1}^2 - 5966u_{i+1}u_i + 2843u_{i+1}^2 + 1922u_{i+1}u_{i-1}, \\ \beta_2 &= 267u_{i-2}^2 - 494u_{i+1}u_{i-2} - 1642u_{i-1}u_{i-2} + 1602u_iu_{i-2} - 5966u_iu_{i-1} + 3443u_i^2 \\ &\quad -2522u_{i+1}u_i + 2843u_{i-1}^2 + 547u_{i+1}^2 + 1922u_{i+1}u_{i-1}, \\ \beta_3 &= 2107u_i^2 + 7042u_iu_{i-2} - 1854u_iu_{i-3} - 9402u_iu_{i-1} - 17246u_{i-1}u_{i-2} + 4642u_{i-1}u_{i-3} + \\ &\quad 547u_{i-3}^2 - 3882u_{i-2}u_{i-3} + 11003u_{i-1}^2 + 7043u_{i-2}^2. \end{aligned}$$

The optimal weights d_l for the left extrapolated value $u_{i+1/2}^L$ at $x_{i+1/2}$ are given by [7]:

$$d_0 = \frac{4}{35}, \quad d_1 = \frac{18}{35}, \quad d_2 = \frac{12}{25}, \quad d_3 = \frac{1}{35} \tag{35}$$

and $u_{i+1/2}^L$ is given by

$$\begin{aligned} u_{i+1/2}^L = u(\xi_{i+1/2} - 0) = \omega_0 \left[\frac{1}{4}u_i + \frac{13}{12}u_{i+1} - \frac{5}{12}u_{i+2} + \frac{1}{12}u_{i+3}\right] + \\ \omega_1 \left[-\frac{1}{12}u_{i-1} + \frac{7}{12}u_i + \frac{7}{12}u_{i+1} - \frac{1}{12}u_{i+2}\right] + \omega_2 \left[\frac{1}{12}u_{i-2} - \frac{5}{12}u_{i-1} + \frac{13}{12}u_i + \frac{1}{4}u_{i+1}\right] + \\ \omega_3 \left[-\frac{1}{4}u_{i-3} + \frac{13}{12}u_{i-2} - \frac{23}{12}u_{i-1} + \frac{25}{12}u_i\right]. \end{aligned} \tag{36}$$

The optimal weights d_l for right boundary extrapolated value $u^R_{i-1/2}$ at $x_{i-1/2}$ are obtained by symmetry

$$d_0 = \frac{1}{35}, \quad d_1 = \frac{12}{25}, \quad d_2 = \frac{18}{35}, \quad d_3 = \frac{4}{35} \tag{37}$$

and $u^R_{i-1/2}$ is given by

$$\begin{gathered} u^R_{i-1/2} = u(\xi_{i-1/2} + 0) = \omega_0 \left[-\frac{1}{4}u_{i+3} + \frac{13}{12}u_{i+2} - \frac{23}{12}u_{i+1} + \frac{25}{12}u_i \right] + \\ \omega_1 \left[\frac{1}{12}u_{i+2} - \frac{5}{12}u_{i+1} + \frac{13}{12}u_i + \frac{1}{4}u_{i-1} \right] + \omega_3 \left[-\frac{1}{12}u_{i+1} + \frac{7}{12}u_i + \frac{7}{12}u_{i-1} - \frac{1}{12}u_{i-2} \right] + \\ \omega_4 \left[\frac{1}{4}u_i + \frac{13}{12}u_{i-1} - \frac{5}{12}u_{i-2} + \frac{1}{12}u_{i-3} \right]. \end{gathered} \tag{38}$$

For the first Gaussian integration point $\xi = \xi_i - \Delta\xi/(2\sqrt{3})$ the optimal weights are as follows:

$$\begin{aligned} d_0 &= \frac{-50\sqrt{3} + 3717}{166320}, & d_1 &= \frac{72\sqrt{3}}{7}\left(\frac{889\sqrt{3}}{63360} - \frac{587}{1995840} \right), \\ d_2 &= \frac{72\sqrt{3}}{7}\left(\frac{889\sqrt{3}}{63360} + \frac{587}{1995840} \right), & d_3 &= \frac{50\sqrt{3} + 3717}{166320} \end{aligned} \tag{39}$$

and the reconstructed value is given by

$$\begin{gathered} u\left(\xi_i - \frac{\Delta\xi}{2\sqrt{3}} \right) = \\ \omega_0 \left[u_i - (-43u_i + 69u_{i+1} - 33u_{i+2} + 7u_{i+3})\frac{\sqrt{3}}{144} - (-u_i + 3u_{i+1} - 3u_{i+2} + u_{i+3})\frac{\sqrt{3}}{432} \right] + \\ \omega_1 \left[u_i - (-15u_i + 27u_{i+1} - 7u_{i-1} - 5u_{i+2})\frac{\sqrt{3}}{144} + (-3u_i + 3u_{i+1} + u_{i-1} - u_{i+2})\frac{\sqrt{3}}{432} \right] + \\ \omega_2 \left[u_i - (15u_i + 7u_{i+1} - 27u_{i-1} + 5u_{i-2})\frac{\sqrt{3}}{144} + (3u_i - u_{i+1} - 3u_{i-1} + u_{i-2})\frac{\sqrt{3}}{432} \right] \\ \omega_3 \left[u_i - (43u_i - 69u_{i-1} + 33u_{i-2} - 7u_{i-3})\frac{\sqrt{3}}{144} - (u_i - 3u_{i-1} + 3u_{i-2} - u_{i-3})\frac{\sqrt{3}}{432} \right]. \end{gathered} \tag{40}$$

For the second Gaussian integration point $\xi = \xi_i + \Delta\xi/(2\sqrt{3})$ optimal weights are obtained from symmetry by interchanging d_0 and d_2:

$$\begin{aligned} d_0 &= \frac{50\sqrt{3} + 3717}{166320}, & d_1 &= \frac{72\sqrt{3}}{7}\left(\frac{889\sqrt{3}}{63360} + \frac{587}{1995840} \right) \\ d_2 &= \frac{72\sqrt{3}}{7}\left(\frac{889\sqrt{3}}{63360} - \frac{587}{1995840} \right), & d_3 &= \frac{-50\sqrt{3} + 3717}{166320}. \end{aligned} \tag{41}$$

The reconstructed value is

$$
\begin{aligned}
& u\left(\xi_i + \frac{\Delta\xi}{2\sqrt{3}}\right) = \\
& \omega_0 \left[u_i + (-43u_i + 69u_{i+1} - 33u_{i+2} + 7u_{i+3})\frac{\sqrt{3}}{144} + (-u_i + 3u_{i+1} - 3u_{i+2} + u_{i+3})\frac{\sqrt{3}}{432} \right] + \\
& \omega_1 \left[u_i + (-15u_i + 27u_{i+1} - 7u_{i-1} - 5u_{i+2})\frac{\sqrt{3}}{144} - (-3u_i + 3u_{i+1} + u_{i-1} - u_{i+2})\frac{\sqrt{3}}{432} \right] \\
& \omega_2 \left[u_i + (15u_i + 7u_{i+1} - 27u_{i-1} + 5u_{i-2})\frac{\sqrt{3}}{144} - (3u_i - u_{i+1} - 3u_{i-1} + u_{i-2})\frac{\sqrt{3}}{432} \right] \\
& \omega_3 \left[u_i + (43u_i - 69u_{i-1} + 33u_{i-2} - 7u_{i-3})\frac{\sqrt{3}}{144} + (u_i - 3u_{i-1} + 3u_{i-2} - u_{i-3})\frac{\sqrt{3}}{432} \right].
\end{aligned}
\tag{42}
$$

3.4 Reconstruction for systems

The reconstruction for systems can be carried out either in conservative variables or in local characteristic variables, see e.g. [7]. For the first option the above expressions (26) – (42) are used for each component of the vector of conservative variables $\mathbf{Q}$. For the characteristic reconstruction one first transforms to characteristic variables and then applies (26) – (42) to each component of these variables. The final values are obtained by transforming back to conservative variables. See [19] for details.

Although the use of characteristic decomposition in reconstruction increases the computational cost of the scheme, our experiments show that in some cases it is necessary in order to avoid spurious oscillations. Our observations agree with those of [16], where the authors use one-dimensional WENO schemes in their experiments. Moreover, in some cases the use of characteristic-wise reconstruction improves overall accuracy of the numerical solution by a factor of two. Therefore, in this paper we always carry out reconstruction in local characteristic variables.

4 Numerical flux

In this section we first briefly review the fluxes to be used in the framework of our schemes. For simplicity we omit subscripts α, β of Gaussian integration points and write $\mathbf{Q}_L \equiv \mathbf{Q}^L_{i+1/2,\alpha\beta}$, $\mathbf{Q}_R \equiv \mathbf{Q}^R_{i+1/2,\alpha\beta}$. We also omit the hat over the numerical flux used as the building block.

4.1 The HLLC flux

The HLLC flux is an improved variant of the HLL flux [9] in that it contains the middle (contact) wave in the Riemann problem solution. It does not use linearization of the equations and works well for low-density problems and sonic points without any fixes. We specialize the presentation of the HLLC flux as applied to the three-dimensional compressible Euler equations

for a gamma-law gas of the form (1) with

$$\mathbf{Q} = \begin{pmatrix} \rho \\ \rho u \\ \rho v \\ \rho w \\ E \end{pmatrix}, \quad \mathbf{F} = \mathbf{Q}u + \begin{pmatrix} 0 \\ p \\ 0 \\ 0 \\ pu \end{pmatrix}, \quad \mathbf{G} = \mathbf{Q}v + \begin{pmatrix} 0 \\ 0 \\ p \\ 0 \\ pv \end{pmatrix}, \quad \mathbf{H} = \mathbf{Q}w + \begin{pmatrix} 0 \\ 0 \\ 0 \\ p \\ pw \end{pmatrix} \tag{43}$$

$$p = (\gamma - 1)(E - \frac{1}{2}\rho(u^2 + v^2 + w^2))$$

where ρ, u, v, w p and E are density, components of velocity in the x, y and z coordinate directions, pressure and total energy, respectively; γ is the ratio of specific heats. An updated version of HLLC for the split 3D Euler equations is found in [25]. Assuming a three-wave structure with wave speed estimates given by S_L, S_* and S_R the HLLC flux is given by

$$\mathbf{F}^{HLLC}_{i+1/2} = \begin{cases} \mathbf{F}_L, & \text{if} \quad 0 \le S_L\,, \\ \mathbf{F}_{*L} = \mathbf{F}_L + S_L(\mathbf{Q}_{*L} - \mathbf{Q}_L)\,, & \text{if} \quad S_L \le 0 \le S_*\,, \\ \mathbf{F}_{*R} = \mathbf{F}_R + S_R(\mathbf{Q}_{*R} - \mathbf{Q}_R)\,, & \text{if} \quad S_* \le 0 \le S_R\,, \\ \mathbf{F}_R, & \text{if} \quad 0 \ge S_R\,, \end{cases} \tag{44}$$

where

$$\mathbf{Q}_{*K} = \rho_K \left(\frac{S_K - u_K}{S_K - S_*}\right) \begin{bmatrix} 1 \\ S_* \\ v_K \\ w_K \\ \frac{E_K}{\rho_K}(S_* - u_K)[S_* + \frac{p_K}{\rho_K(S_K - u_K)}] \end{bmatrix}$$

for $K = L$ and $K = R$. The wave speeds S_L, S_* and S_R must be estimated. We use the pressure-velocity estimates of Sect. 10.5.2 of [25].

4.2 The FORCE flux

The FORCE flux [24, 25] is a recent centred flux which is derived as the deterministic version of the staggered-grid Random Choice Method:

$$\begin{aligned} \mathbf{F}^{FORCE}_{i+1/2}(\mathbf{Q}_L, \mathbf{Q}_R) &= \frac{1}{4}\left(\mathbf{F}_L + 2\mathbf{F}(\mathbf{Q}^{1/2}) + \mathbf{F}_R - \frac{\Delta x}{\Delta t}(\mathbf{Q}_R - \mathbf{Q}_L)\right), \\ \mathbf{Q}^{1/2} &= \frac{1}{2}(\mathbf{Q}_L + \mathbf{Q}_R) - \frac{1}{2}\frac{\Delta t}{\Delta x}(\mathbf{F}_R - \mathbf{F}_L). \end{aligned} \tag{45}$$

It turns out that the above flux is an arithmetic mean of the Lax-Friedrichs and Law-Wendroff fluxes. It can be shown [24, 25, 3] that the numerical viscosity of the FORCE flux is smaller than that of the Lax-Friedrichs flux by a factor of two. The FORCE flux has been successfully used in the construction of centred multidimensional *non-staggered mesh* TVD schemes [27, 28]. Recently the FORCE scheme has been shown to be convergent for some 2×2 non-linear systems of hyperbolic conservation laws [3].

4.3 Upwind MUSTA fluxes

In general, the good accuracy of Godunov-type fluxes results from the opening of the Riemann fan and picking up a single value at cell interface $x_{i+1/2}$. Complete (exact or approximate) Riemann solvers recognize all waves in the Riemann fan and therefore provide good resolution of delicate features of the flow, such as contact discontinuities and shear waves. Incomplete Riemann solvers (e.g. HLL flux [9]) do not recognize the intermediate waves in the Riemann fun and lump them all in one (averaged) state. Centred fluxes can be regarded as very rough Riemann solvers in which the Riemann fan is not opened at all. As a result, the resolution of all intermediate waves and associated flow features by incomplete and centred fluxes is very poor; e.g. contact discontinuities are smeared in time considerably.

A very simple and general approach to the construction of numerical fluxes, which combines the simplicity of centred fluxes and the good accuracy of the Godunov method, is the Multi-Stage (MUSTA) approach [26]. The MUSTA approach develops upwind numerical fluxes by utilising centred fluxes in a multi-stage predictor-corrector fashion. Effectively, MUSTA can be regarded as an approximate Riemann solver in which the predictor step opens the Riemann fan and the corrector step makes use of the information extracted from the opened Riemann fan, which is precisely the information needed for the upwind numerical flux. The advantages of this multi-stage predictor-corrector solver are its simplicity and generality and will be fully realised when solving very complex hyperbolic systems such as those arising in multi-phase flows, magnetohydrodynamics and general relativity.

The key idea of MUSTA is to open the Riemann fun by solving the local Riemann problem numerically rather than analytically. Suppose we have a mesh of p cells to the left of $x_{i+1/2}$ and p cells to the right of $x_{i+1/2}$ and we solve the local Riemann problem on this mesh. At every time step l we have the discrete values of $\mathbf{Q}$ corresponding to these cells. If for some l the vectors adjacent to the interface, namely $\mathbf{Q}_L^{(l)}$ and $\mathbf{Q}_R^{(l)}$, are close

$$|\mathbf{Q}_L^{(l)} - \mathbf{Q}_R^{(l)}| \leq \varepsilon,$$

where $||$ is a suitable norm and $\varepsilon > 0$ is a small tolerance, one would stop the time-marching procedure. The two vectors of interest now are the final values $\mathbf{Q}_L^{(k)}$, $\mathbf{Q}_R^{(k)}$. It is likely that these values for large k are identical. They will be different if they are separated by a stationary discontinuity or a transonic rarefaction. In the MUSTA approach the existing discontinuity is resolved by applying in the corrector step a simple flux, such as a centred flux:

$$\mathbf{F}_{i+1/2}^{(k)} = \mathbf{F}(\mathbf{Q}_L^{(k)}, \mathbf{Q}_R^{(k)}). \tag{46}$$

It turns out that for practical purposes it is sufficient to take $p = 1$ and a small number of stages k. A particularly successful flux, constructed on the basis of the centred FORCE flux, is summarised here. It has essentially two steps and is started by setting $l = 1$, $\mathbf{Q}_L^{(1)} = \mathbf{Q}_L$ and $\mathbf{Q}_R^{(1)} = \mathbf{Q}_R$. Then we do

1. Flux evaluation

$$\begin{aligned}
&\mathbf{F}_L^{(l)} = \mathbf{F}(\mathbf{Q}_L^{(l)}), \quad \mathbf{F}_R^{(l)} = \mathbf{F}(\mathbf{Q}_R^{(l)}), \\
&\mathbf{Q}_M^{(l)} = \frac{1}{2}\left[\mathbf{Q}_L^{(l)} + \mathbf{Q}_R^{(l)}\right] - \frac{1}{2}\frac{\Delta t}{\Delta x}\left[\mathbf{F}_R^{(l)} - \mathbf{F}_L^{(l)}\right], \quad \mathbf{F}_M^{(l)} = \mathbf{F}(\mathbf{Q}_M^{(l)}) \\
&\mathbf{F}_{i+1/2}^{(l)} = \frac{1}{4}\left(\mathbf{F}_L^{(l)} + 2\mathbf{F}_M^{(l)} + \mathbf{F}_R^{(l)} - \frac{\Delta x}{\Delta t}\left(\mathbf{Q}_R^{(l)} - \mathbf{Q}_L^{(l)}\right)\right),
\end{aligned} \tag{47}$$

2. Open Riemann fun

$$\mathbf{Q}_L^{(l+1)} = \mathbf{Q}_L^{(l)} - \frac{\Delta t}{\Delta x}\left[\mathbf{F}_{i+1/2}^{(l)} - \mathbf{F}_L^{(l)}\right], \quad \mathbf{Q}_R^{(l+1)} = \mathbf{Q}_R^{(l)} - \frac{\Delta t}{\Delta x}\left[\mathbf{F}_R^{(l)} - \mathbf{F}_{i+1/2}^{(l)}\right]. \tag{48}$$

3. Goto to step 1

The procedure is stopped at the end of Step 1 if the desired number of stages k has been reached. Practical experience suggests that a number of stages between 3 and 4 gives numerical results that are comparable with those from the most accurate of fluxes, namely, the first-order Godunov upwind flux used in conjunction with the exact Riemann solver [26]. In this paper we use $k = 4$ throughout unless otherwise stated.

Concerning efficiency, it is found that, for the one-dimensional Euler equations for ideal gases, the cost of such a flux is comparable to that of typical existing approximate Riemann solvers, such as the HLLC [29] or Roe [17] solvers. Moreover, in WENO schemes the reconstruction step accounts for most of the computational cost so that the difference in the cost between the HLLC, FORCE and MUSTA fluxes becomes negligible.

5 Numerical results

In this section we present numerical results for the scalar advection equation and compressible Euler equations in one, two and three space dimensions. For the scalar equations the HLLC flux is equivalent to the Godunov flux with the exact Riemann solver; therefore we call the corresponding scheme the WENO-Exact scheme. Our experience suggests that for most cases the accuracy of the third order Runge-Kutta method (10) is comparable with that of the forth order Runge-Kutta method of [21] whereas the third order method has a lower computational cost and requires less memory as well. Therefore we use (10) throughout, unless otherwise stated.

An important issue is the choice of the Courant number defining the time step. We remark that it seems to have become a popular practice to demonstrate the formal order of spatial accuracy of WENO schemes by choosing the time step in such a way that the spatial order dominates the computation. For example, when the third order Runge-Kutta method (10) is used the time step is chosen according to

$$\Delta t \approx \Delta x^{(2r-1)/3}. \tag{49}$$

We have run our schemes with such a time step and obtained good results. However, it should be noted that the use of (49) results in exceedingly small time steps and therefore *enormous* computational cost of the scheme. This is especially so in multiple space dimensions. For example, take $r = 4$, then (49) becomes $\Delta t \approx \Delta x^{7/3}$ which is more stringent than the stability condition for parabolic equations.

For hyperbolic equations the natural choice of the time step is the one resulting from the use of a fixed Courant number. From the point of efficiency it should be as close as possible to the maximum range allowed by the stability condition (12) – (14). In this paper our goal is to assess the performance of our methods as they will be used in practical computations. We run all convergence tests with a fixed Courant number, which is chosen to be $C_{cfl} = 0.45$ in two space dimensions and $C_{cfl} = 0.27$ in three space dimensions.

5.1 Scalar equations

5.1.1 Linear advection equation

We solve the one-dimensional linear advection equation

$$q_t + \lambda\, q_x = 0, \quad \lambda = 1 \tag{50}$$

with the following initial condition [7, 22, 1] defined on on $[-1:1]$:

$$q(x,0) = \begin{cases} \exp\left(\ln 2\,(x+0.7)^2/0.0009\right), & -0.8 \le x \le -0.6 \\ 1, & -0.4 \le x \le -0.2 \\ 1-|10x-1|, & 0.0 \le x \le 0.2 \\ (1-100(x-0.5)^2)^{1/2}, & 0.4 \le x \le 0.6 \\ 0, & \text{otherwise} \end{cases} \tag{51}$$

This initial condition consists of a discontinuous square pulse and several continuous but narrow profiles. We apply periodic boundary conditions. The Courant number of 0.4 is used for all runs.

Table 1 shows a convergence study for output times $t = 10$ and $t = 1000$ for schemes with piece-wise parabolic ($r = 3$) WENO reconstruction. We present the errors and convergence rates for *cell averages* of the solution in the L_1 norm; in this norm the first order of accuracy should be achieved even for the discontinuous solutions. We observe that for the first (small) output time all schemes converge with the expected order of accuracy and produce similar errors; the influence of the numerical flux used as the building block is small. For the second, much larger time, the choice of the flux affects the accuracy much more strongly. As expected, the scheme with the centred FORCE flux is the least accurate scheme. The WENO-Exact scheme performs slightly better. The most accurate scheme for this output time is the WENO-MUSTA scheme: on the finest mesh it is roughly four time more accurate than the WENO-FORCE scheme.

Further illustration is provided by Fig. 1, which depicts numerical solutions of all schemes at the output time $t = 1000$ on the finest mesh of 1600 cells. In full accordance with Table 1 the accuracy improves as we go from the WENO-FORCE scheme to the WENO-Exact and then to the WENO-MUSTA scheme. The WENO-FORCE scheme diffuses all profiles in the numerical solution except the very smooth Gaussian part of the initial condition. The WENO-Exact scheme resolves well not only the Gaussian curve but also the triangle and provides a reasonable result for the semi-circular profile. The most accurate scheme is the WENO-MUSTA scheme which resolves well all profiles in the solution.

The example demonstrates the importance of using long time evolution test problems in assessing the performance of different methods. For small output times all methods produce similar results and the real difference in accuracy becomes apparent only when the solution is evolved for a sufficiently large time.

5.1.2 The kinematic frontogenesis problem

This test problem [4] is important in meteorology where it represents a simplified effect which takes place in the atmosphere. From the numerical point of view it tests the ability of the

schemes to handle moving discontinuities in two space dimensions. We remark that a number of advection schemes has been reported to fail for this test problem, especially those using dimensional splitting.

We solve the two-dimensional linear equation with variable coefficients

$$q_t + (u(x,y)q)_x + (v(x,y)q)_y = 0 \tag{52}$$

where (u, v) is a steady divergence-free velocity field:

$$\begin{gathered} u = -y\,\omega(r), \quad v = x\,\omega(r), \quad \omega(r) = \frac{1}{r}U_T(r), \quad r^2 = x^2 + y^2, \\ U_T(r) = U_{max}\mathrm{sech}^2(r)\tanh(r), \quad U_{max} = 2.5980762. \end{gathered} \tag{53}$$

We solve (52) - (53) with the following initial condition defined on $[-5, 5] \times [-5, 5]$:

$$q(x,y,0) = \begin{cases} -1, & y < 0 \\ 1, & y > 0 \end{cases} \tag{54}$$

The exact solution is then given by [4]

$$q(x,y,t) = q_0(y\cos(\omega t) - x\sin(\omega t)) \tag{55}$$

and represents a rotation of the initial discontinuous distribution around the origin with variable angular velocity $\omega(r)$. We note that as time evolves the solution will eventually develop scales which will be beyond the resolution of the computational mesh.

We compute the numerical solution for the output time $t = 4$ using the meshes of 201×201 and 401×401 cells. Figures (2) – (4) show one-dimensional cuts along the y axis for $-3 \le y \le 3$ for schemes with piece-wise parabolic reconstruction. In all figures the solid line corresponds to the point-wise values of the exact solution whereas symbols correspond to the numerical solution (cell averages). Clearly all schemes capture delicate features of the solution correctly without oscillations. The WENO-Exact and WENO-MUSTA produce results of similar accuracy whereas the WENO-FORCE is a little bit more diffusive.

Further illustration is provided by Fig. 5 which depicts the three-dimensional plot of the numerical solution obtained by the WENO-MUSTA scheme. We observe that the numerical solution is monotone with sharp resolution of all discontinuities.

5.1.3 The three-dimensional inviscid Burgers' equation

We solve the three-dimensional inviscid Burgers' equation

$$q_t + \left(\frac{1}{2}q^2\right)_x + \left(\frac{1}{2}q^2\right)_y + \left(\frac{1}{2}q^2\right)_z = 0 \tag{56}$$

with the following initial condition defined on $[-1, 1] \times [-1, 1] \times [-1, 1]$:

$$q(x,y,z,0) = q_0(x,y,z) = 0.25 + \sin(\pi x)\sin(\pi y)\sin(\pi z) \tag{57}$$

and periodic boundary conditions. For this test problem the exact solution is obtained by solving numerically the relation $q = q_0(x - qt, y - qt, z - qt)$ for a given point (x, y, z) and time t. The cell averages of the exact solution at the output time are computed using the 8^{th}-order Gaussian rule.

Table 2 shows the errors of WENO schemes with the piece-wise parabolic and cubic reconstructions at the output time $t = 0.05$, when the solution is still smooth. The forth order strong–stability preserving (SSP) Runge-Kutta method [21] and a fixed Courant number $C_{cfl} = 0.27$ are used. We observe that approximately fifth order of accuracy is reached by all schemes, which actually well exceeds the expected forth order of accuracy which should result from the use of the two-point Gaussian quadrature (23). For a fixed resolution the schemes with cubic reconstruction are more accurate than the corresponding schemes with parabolic reconstruction. Since the same forth order Runge-Kutta method is used for time discretization we conclude that on the given meshes the spatial error dominates.

The effect of using even higher order reconstructions is illustrated in Table 3 which shows the convergence study for schemes with the piece-wise quadric ($r = 5$) and piece-wise quintic ($r = 6$) reconstructions. To save space we show only the results corresponding to the use of the most accurate four-point Gaussian quadrature in (7). We observe that overall, increasing the spatial order of accuracy still decreases the error. However, the gains are much smaller than those in Table 2 and for $r = 6$ may not justify the considerable increase in the computation cost, since there is virtually no difference between the results of schemes with piece-wise quintic and quadric reconstructions. On fine meshes the convergence rates drops to the forth order expected from the use of the forth order Runge-Kutta method for time evolution. Therefore, the spatial error no longer dominates and increasing the order of reconstruction polynomials even further will not improve results.

The influence of the numerical flux used as a building block is most visible for lower order reconstructions ($r = 3, 4$) and coarse meshes; e.g. compare results of WENO-FORCE and WENO-MUSTA schemes in Table 3 for the coarsest mesh of 10 cells in each coordinate direction. With increasing spatial orders and mesh resolution the difference becomes negligible; the schemes in Table 3 on the finest mesh produce almost identical errors.

5.2 Compressible Euler equations

In this section we evaluate the accuracy and robustness of our methods as applied to three test problems.

5.2.1 Modified shock/turbulence interaction

This test problem is a variation of the shock/turbulence problem used in [7, 1]. We solve the Euler equations (43) with the following initial condition defined on $[-5, 5]$

$$(\rho, u, p) = \begin{cases} (1.515695, 0.523346, 1.80500), & x < -4.5 \\ (1 + 0.1 \sin 20\pi x, 0.0, 1.), & x > -4.5 \end{cases} \tag{58}$$

which consists of a right facing shock wave of Mach number 1.1 impinging into a high-frequency density perturbation. As the shock moves the perturbation spreads upstream. We compute the flow at the output time $t = 5$ which is more than ten times larger than that of the standard shock/turbulence problem [1]. The solution contains physical oscillations which have to be resolved by the numerical method.

Fig. 6 shows results of all schemes on a mesh of 2000 cells. The Courant number $C_{cfl} = 0.6$ is used. In all figures symbols denote the numerical solution and the solid line denotes the reference solution computed on a fine mesh of 5000 cells using the fifth order ADER-WAF

scheme [30]. We see that on the given mesh the centred WENO-FORCE severely damps the acoustic disturbance which spreads upstream of the shock. The WENO-HLLC scheme produces much more accurate results and WENO-MUSTA is the most accurate scheme for the given CFL number and mesh.

5.2.2 Two-dimensional vortex evolution problem

We solve the two-dimensional Euler equations with the initial conditions, corresponding to a smooth vortex, moving at 45^o to the Cartesian mesh lines. This test problem is from [1] where it is used to study the convergence properties of finite-difference WENO schemes. The problem is solved in the square domain $[-5:5]\times[-5:5]$ with periodic boundary conditions. The vortex is defined as the following isentropic perturbation to the uniform flow of unit values of primitive variables:

$$\begin{gathered} u = 1 - \frac{\varepsilon}{2\pi} e^{\frac{1}{2}(1-r^2)}\, y, \quad v = 1 + \frac{\varepsilon}{2\pi} e^{\frac{1}{2}(1-r^2)}\, x, \\ T = 1 - \frac{(\gamma-1)\varepsilon^2}{8\gamma\pi^2} e^{(1-r^2)}, \quad \frac{p}{\rho^\gamma} = 1, \end{gathered} \tag{59}$$

where $r^2 = x^2 + y^2$ and the vortex strength is $\varepsilon = 5$. We compute the numerical solution at the output time $t = 10$ which corresponds to one time period; at this time the vortex returns to the initial position. We use $C_{cfl} = 0.45$ for all runs.

Table 4 shows the convergence study for schemes with piece-wise parabolic ($r = 3$) and piece-wise cubic ($r = 4$) reconstructions. We observe that approximately fifth order of accuracy is achieved by all schemes. This order is higher than expected from the use of the third order Runge-Kutta method due to the fact that this problem, *for the given output time*, is more sensitive to spatial accuracy rather than time discretization. For a fixed resolution the accuracy of the schemes with piece-wise cubic reconstruction is higher by a factor of ten. Table 5 shows the convergence study for schemes with higher order piece-wise quartic ($r = 5$) and piece-wise quintic ($r = 6$) reconstructions. As before, the accuracy is improved as we go from lower order polynomials to higher order ones. However, the difference becomes smaller as the order of the reconstruction polynomials grows.

The influence of the particular flux being used as a building block in the scheme is quite significant for the schemes in Table 4, even though the solution is infinitely smooth, but almost disappears in the results of Table 5. Again, the WENO-MUSTA scheme is the most accurate scheme.

We have also run a three-dimensional vortex problem with the initial conditions, corresponding to a smooth vortex (59), placed in the $y - z$ plane. The results are essentially the same as in the two-dimensional case and are thus omitted.

5.2.3 Three-dimensional explosion test problem

Finally, we solve the three-dimensional Euler equations of a gamma law gas (1), (43). The initial condition defined on $[-1:1]\times[-1:1]\times[-1:1]$ consists of two regions of constant but different values of gas parameters separated by a sphere of radius 0.4:

$$(\rho, p) = \begin{cases} (1.0,\ 1.0), & r \le 0.4 \\ (0.125,\ 0.1), & r > 0.4 \end{cases}, \quad u = v = w = 0, \quad r^2 = x^2 + y^2 + z^2. \tag{60}$$

This initial condition corresponds to the so-called spherical explosion test problem [25]. We compute the numerical solution at the output time $t = 0.25$ on a mesh of 101 cells in each coordinate direction. We use $C_{cfl} = 0.27$ for all runs. We compare the results of the WENO schemes with a reference radial solution, which is obtained by solving the one-dimensional Euler equations with a geometrical source term on a very fine mesh, see Section 17.1 of [25] for details.

Figs. 7 – 9 show a comparison between the one-dimensional reference radial solution (solid line) and the cell averages of the three-dimensional WENO solution (symbols) along the radial line that is coincident with the x-axis. We present distributions of gas density ρ and internal energy e. The solution contains a spherical shock wave and a contact surface travelling away from the centre and a spherical rarefaction wave travelling towards the origin (0,0,0). We observe that all schemes obtain the right solution with the correct values behind the shock wave and the contact surface. The influence of the numerical flux used as the building block is quite clear here: compared to the centred WENO-FORCE scheme the upwind WENO-HLLC and WENO-MUSTA produce much sharper profiles of virtually all flow features.

Figs. 10 – 11 show the density and internal energy distribution on the plane $z = 0$ for the WENO-MUSTA scheme. We observe that the numerical solution is monotone with sharp profiles of all discontinuities.

6 Conclusions

In this paper we first carried out an extension of the existing finite-volume WENO schemes to three space dimensions and up to 11^{th} order of spatial accuracy. We provided all necessary information for the reconstruction step of most practical fifth and seventh order schemes, so that the schemes can be easily coded.

Secondly we proposed to use the FORCE, HLLC and MUSTA fluxes as the building block in the WENO schemes. The upwind HLLC and centred FORCE fluxes are conventional (one-stage) fluxes which have successfully been used in the past for the construction of TVD schemes. The MUSTA flux is a very recent multi-stage upwind flux which does not need any information on the details of Riemann problem solution. It combines the good accuracy of the upwind fluxes based on complete Riemann solvers and the simplicity of centred fluxes.

We presented the numerical results of the new WENO-FORCE, WENO-HLLC and WENO-MUSTA schemes in one, two and three space dimensions. They suggest that the proposed schemes achieve uniformly high order of accuracy for smooth solutions and produce essentially non-oscillatory profiles for discontinuities. We observe significant improvements in accuracy as we go from fifth order to higher orders of spatial reconstruction as well as from the centred to the upwind fluxes.

A particularly useful scheme is the WENO-MUSTA scheme coupled with fifth or seventh order reconstruction. This scheme combines the simplicity of centred WENO schemes and accuracy of upwind WENO schemes with complete Riemann solvers. The advantages of the WENO-MUSTA scheme will be fully realised when solving very complex hyperbolic systems such as those arising in multi-phase flows, magnetohydrodynamics and general relativity.

Future developments will include extension of the WENO-MUSTA scheme to unstructured meshes.

Acknowledgments. The paper was finalized during the stay of the first author at the

Isaac Newton Institute for Mathematical Sciences, University of Cambridge and participation in the programme *Nonlinear Hyperbolic Waves in Phase Dynamics and Astrophysics*. The second author acknowledges the support provided by the Isaac Newton Institute for Mathematical Sciences, University of Cambridge, UK, as organizer of the six-month programme on *Nonlinear Hyperbolic Waves in Phase Dynamics and Astrophysics*, January to July 2003, and the associated EPSRC senior visiting fellowship, grant No GR N09276.

References

[1] Balsara D. S. and Shu C.W. (2000). Monotonicity preserving weighted essentially non-oscillatory schemes with increasingly high order of accuracy. *J. Comp. Phys.*, **160**, pp. 405-452.

[2] Casper J. and Atkins H. (1993). A finite-volume high order ENO scheme for two dimensional hyperbolic systems. *J. Comp. Phys.*, **106**, pp. 62-76.

[3] Chen G.Q. and Toro E.F. (2003). Centred schemes for nonlinear hyperbolic equations. Preprint NI03046-NPA. Isaac Newton Institute for Mathematical Sciences, University of Cambridge, UK. - 2003. – 31 P., submitted.

[4] Davies-Jones R. (1985). Comments on 'A kinematic analysis of frontogenesis associated with a non-divergent vortex'. *J. Atm. Sci.*, **42**, pp. 2073-2075.

[5] Godunov S. K. (1959). A finite difference method for the computation of discontinuous solutions of the equation of fluid dynamics. *Mat. Sb.*, **47**, pp. 357-393.

[6] Grasso F. and Pirozzoli S. (2000). Shock wave - thermal inhomogeneity interactions: analysis and numerical simulations of sound generation. *Physics of Fluids*, **12**, N. 1, pp. 205–219.

[7] Jiang G.S. and Shu C.W. (1996). Efficient implementation of weighted ENO schemes. *J. Comput. Phys.*, **126**, pp. 202-212.

[8] Harten A., Engquist B., Osher S. and Chakravarthy S.R. (1987) Uniformly high order accurate essentially non-oscillatory schemes III. *J. Comput. Phys.*, **71**, pp. 231-303.

[9] Harten A., Lax P. D. and van Leer B. (1983). On upstream differencing and Godunov-type schemes for hyperbolic conservation laws. *SIAM Review*, **25**, N. 1, pp. 35-61.

[10] Hu C. and Shu C.-W. (1999). Weighted essentially non-oscillatory schemes on triangular meshes. *J. Comp. Phys.*, **150**, pp. 97-127.

[11] Kolgan N.E. (1972). Application of the minimum-derivative principle in the construction of finite-difference schemes for numerical analysis of discontinuous solutions in gas dynamics. *Uchenye Zapiski TsaGI* [Sci. Notes of Central Inst. of Aerodynamics], **3**, No. 6, pp. 68-77 (in Russian).

[12] Kolgan N.E. (1975). Finite-difference schemes for computation of three dimensional solutions of gas dynamics and calculation of a flow over a body under an angle of attack. *Uchenye Zapiski TsaGI* [Sci. Notes of Central Inst. of Aerodynamics], **6**, No. 2, pp. 1-6 (in Russian).

[13] Levy D., Puppo G. and Russo G. (1999). Central WENO schemes for hyperbolic systems of conservation laws. *Mathematical Modelling and Numerical Analysis*, **33**, N. 3, 1999, pp. 547-571.

[14] Levy D., Puppo G. and Russo G. (2002). A forth order central WENO scheme for multi-dimensional hyperbolic systems of conservation laws. *SIAM Journal of Scientific Computing*, **22**, pp. 480-506.

[15] Liu X.D., Osher S. and Chan T. (1994). Weighted essentially non-oscillatory schemes. *J. Comput. Phys.*, **115**, pp. 200-212.

[16] Qiu J. and Shu C.-W. (2002) On the construction, comparison, and local characteristic decomposition for high order central WENO schemes. *J. Comp. Phys.*, **183**, pp. 187-209.

[17] Roe P.L. (1981). Approximate Riemann solvers, parameter vectors, and difference schemes. *J. Comp. Phys.*, **43**, pp. 357-372.

[18] Rusanov V.V. (1961). Calculation of interaction of non-steady shock waves with obstacles. *J. Comp. Math. Phys., USSR*, **1**, pp. 267-279.

[19] Shi J., Hu C. and Shu C.-W. (2002). A technique for treating negative weights in WENO schemes. *J. Comp. Phys.*, **175**, pp. 108-127.

[20] Shu C.-W. (1988). Total - Variation - Diminishing time discretizations. *SIAM J. Scientific and Statistical Computing*, **9**, pp. 1073-1084.

[21] Spitery R. J. and Ruuth S.J. (2002). A new class of optimal high-order strong-stability-preserving time discretization methods. *SIAM J. Numer. Anal.*, **40**, N 2, pp. 469-491.

[22] Suresh A. and Huynh T. (1997). Accurate monotonicity preserving scheme with Runge-Kutta time stepping. *J. Comput. Phys*, **136**, pp. 83-99.

[23] Toro E.F. (1989). A weighted average flux method for hyperbolic conservation laws. *Proceedings of the Royal Society of London*, A 423, pp 401-418.

[24] Toro E.F. (1996). On Glimm-related schemes for conservation laws. Technical Report MMU-9602, Department of Mathematics and Physics, Manchester Metropolitan University, UK.

[25] Toro E.F. (1999). *Riemann Solvers and Numerical Methods for Fluid Dynamics*. Second Edition, Springer-Verlag.

[26] Toro E.F. (2003). Multi-stage predictor-corrector fluxes for hyperbolic equations. Preprint NI03037-NPA. Isaac Newton Institute for Mathematical Sciences, University of Cambridge, UK, *submitted to J. Comp. Phys.*

[27] Toro E. F. and Billett S. J. (2000). Centred TVD Schemes for Hyperbolic Conservation Laws. *IMA J. Numerical Analysis*, **20**, pp. 47-79.

[28] Toro E F and Hu W (2001). Centred Unsplit Finite Volume Schemes for Hyperbolic Conservation Laws. In Godunov Methods: Theory and Applications, Edited Review, Toro E F (Editor), Kluwer Academic/Plenum Publishers, pp. 897-902, 2001.

[29] Toro E.F., Spruce M. and Speares W. (1994). Restoration of the Contact Surface in the Harten-Lax-van Leer Riemann Solver. *Journal of Shock Waves*, **4**, pp. 25-34.

[30] Toro E.F and Titarev V.A. (2003). TVD Fluxes for the High-Order ADER Schemes, Preprint NI03011-NPA. Isaac Newton Institute for Mathematical Sciences, University of Cambridge, UK. - 2003. – 37 P., submitted.

[31] van Leer B. (1979). Towards the ultimate conservative difference scheme V: a second order sequel to Godunov' method. *J. Comput. Phys.* **32**, pp. 101-136.

Table 1: Convergence study for the 1D linear advection equation (50) with initial condition (51) at the output time $t = 10$. WENO schemes with piece-wise parabolic reconstruction. $C_{cfl} = 0.4$ is used for all schemes. N denotes the number of cells in the mesh.

Scheme	N	L_1 error	L_1 order	L_1 error	L_1 order
		$t = 10$		$t = 1000$	
WENO-FORCE	100	2.22×10^{-1}		6.06×10^{-1}	
	200	1.03×10^{-1}	1.11	3.97×10^{-1}	0.61
	400	4.51×10^{-2}	1.19	4.70×10^{-1}	-0.24
	800	2.16×10^{-2}	1.06	3.83×10^{-1}	0.30
	1600	1.16×10^{-2}	0.90	2.29×10^{-1}	0.74
WENO-Exact	100	2.09×10^{-1}		5.76×10^{-1}	
	200	9.42×10^{-2}	1.15	3.36×10^{-1}	0.78
	400	4.12×10^{-2}	1.19	3.05×10^{-1}	0.14
	800	1.98×10^{-2}	1.06	2.14×10^{-1}	0.51
	1600	1.04×10^{-2}	0.93	1.11×10^{-1}	0.95
WENO-MUSTA	100	1.99×10^{-1}		5.50×10^{-1}	
	200	8.81×10^{-2}	1.18	3.00×10^{-1}	0.87
	400	3.86×10^{-2}	1.19	2.07×10^{-1}	0.54
	800	1.87×10^{-2}	1.05	1.06×10^{-1}	0.97
	1600	9.75×10^{-3}	0.94	5.25×10^{-2}	1.01

Table 2: Convergence study for the 3D inviscid Burgers' equation (56) with initial condition (57) at output time $t = 0.05$. $C_{cfl} = 0.27$ and forth order RK method [21] are used for all schemes. The two-point Gaussian quadrature is used for all schemes. N is the number of cells in each coordinate direction.

Method	N	L_∞ error	L_∞ order	L_1 error	L_1 order
WENO schemes with piece-wise parabolic ($r = 3$) reconstruction					
WENO-FORCE	10	1.46×10^{-2}		3.59×10^{-2}	
	20	1.20×10^{-3}	3.61	1.37×10^{-3}	4.71
	40	4.40×10^{-5}	4.77	3.81×10^{-5}	5.17
WENO-Exact	10	4.33×10^{-3}		4.06×10^{-3}	
	20	3.19×10^{-4}	3.76	1.86×10^{-4}	4.45
	40	1.48×10^{-5}	4.43	7.03×10^{-6}	4.72
WENO-MUSTA	10	4.21×10^{-3}		5.72×10^{-3}	
	20	3.23×10^{-4}	3.70	2.06×10^{-4}	4.80
	40	1.20×10^{-5}	4.75	5.91×10^{-6}	5.12
WENO schemes with piece-wise cubic ($r = 4$) reconstruction					
WENO-FORCE	10	9.48×10^{-3}		6.99×10^{-3}	
	20	2.20×10^{-4}	5.43	9.69×10^{-5}	6.17
	40	2.73×10^{-6}	6.34	1.18×10^{-6}	6.36
WENO-Exact	10	2.90×10^{-3}		7.94×10^{-4}	
	20	6.57×10^{-5}	5.47	1.97×10^{-5}	5.33
	40	2.04×10^{-6}	5.01	7.28×10^{-7}	4.76
WENO-MUSTA	10	3.06×10^{-3}		1.25×10^{-3}	
	20	5.62×10^{-5}	5.77	2.28×10^{-5}	5.77
	40	1.84×10^{-6}	4.93	7.32×10^{-7}	4.96

Table 3: Convergence study for the 3D inviscid Burgers' equation (56) with initial condition (57) at output time $t = 0.05$. $C_{cfl} = 0.27$ and forth order RK method [21] are used for all schemes. The four-point Gaussian quadrature is used for all schemes. N is the number of cells in each coordinate direction.

Method	N	L_∞ error	L_∞ order	L_1 error	L_1 order
WENO schemes with piece-quadric ($r = 5$) reconstruction					
WENO-FORCE	10	3.14×10^{-3}		3.06×10^{-3}	
	20	2.63×10^{-5}	6.90	2.21×10^{-5}	7.11
	40	1.08×10^{-6}	4.61	2.45×10^{-7}	6.50
WENO-Exact	10	1.97×10^{-4}		2.53×10^{-4}	
	20	1.26×10^{-5}	3.98	3.58×10^{-6}	6.14
	40	1.09×10^{-6}	3.53	2.26×10^{-7}	3.99
WENO-MUSTA	10	3.63×10^{-4}		4.55×10^{-4}	
	20	1.35×10^{-5}	4.75	4.89×10^{-6}	6.54
	40	1.09×10^{-6}	3.63	2.28×10^{-7}	4.43
WENO schemes with piece-wise quintic ($r = 6$) reconstruction					
WENO-FORCE	10	2.21×10^{-3}		1.90×10^{-3}	
	20	1.18×10^{-5}	7.55	9.17×10^{-6}	7.70
	40	1.08×10^{-6}	3.44	2.29×10^{-7}	5.32
WENO-Exact	10	2.37×10^{-4}		1.66×10^{-4}	
	20	1.44×10^{-5}	4.03	3.44×10^{-6}	5.59
	40	1.08×10^{-6}	3.74	2.29×10^{-7}	3.91
WENO-MUSTA	10	3.32×10^{-4}		3.00×10^{-4}	
	20	1.48×10^{-5}	4.48	3.87×10^{-6}	6.28
	40	1.08×10^{-6}	3.78	2.29×10^{-7}	4.08

Table 4: Density convergence study for the vortex evolution problem (59) at the output time $t = 10$. WENO schemes with piece-wise parabolic ($r = 3$) reconstruction. N denotes the number of cells in each coordinate direction. $C_{cfl} = 0.45$ is used for all schemes.

Method	N	L_∞ error	L_∞ order	L_1 error	L_1 order
WENO schemes with piece-wise parabolic ($r = 3$) reconstruction					
WENO-FORCE	25	1.45×10^{-1}		9.78×10^{-3}	
	50	1.75×10^{-2}	3.05	6.89×10^{-4}	3.83
	100	6.16×10^{-4}	4.83	3.58×10^{-5}	4.26
WENO-HLLC	25	6.62×10^{-2}		3.86×10^{-3}	
	50	9.89×10^{-3}	2.74	2.76×10^{-4}	3.81
	100	2.68×10^{-4}	5.21	1.24×10^{-5}	4.47
WENO-MUSTA	25	5.09×10^{-2}		3.53×10^{-3}	
	50	8.63×10^{-3}	2.56	2.28×10^{-4}	3.95
	100	2.17×10^{-4}	5.32	9.41×10^{-6}	4.60
WENO schemes with piece-wise cubic ($r = 4$) reconstruction					
WENO-FORCE	25	3.72×10^{-2}		2.42×10^{-3}	
	50	3.36×10^{-3}	3.47	1.33×10^{-4}	4.18
	100	7.88×10^{-5}	5.41	3.88×10^{-6}	5.10
WENO-HLLC	25	2.08×10^{-2}		1.62×10^{-3}	
	50	9.58×10^{-4}	4.44	5.08×10^{-5}	5.00
	100	3.41×10^{-5}	4.81	1.56×10^{-6}	5.02
WENO-MUSTA	25	2.85×10^{-2}		2.69×10^{-3}	
	50	7.74×10^{-4}	5.20	4.30×10^{-5}	5.97
	100	2.83×10^{-5}	4.77	1.30×10^{-6}	5.04

Table 5: Density convergence study for the vortex evolution problem (59) at the output time $t = 10$. The four-point Gaussian quadrature is used for flux integration over cell sides. N denotes the number of cells in each coordinate direction. $C_{cfl} = 0.45$ is used for all schemes.

Method	N	L_∞ error	L_∞ order	L_1 error	L_1 order
WENO schemes with piece-wise quadric ($r = 5$) reconstruction.					
WENO-FORCE	25	2.46×10^{-2}		1.14×10^{-3}	
	50	7.60×10^{-4}	5.02	3.61×10^{-5}	4.99
	100	1.49×10^{-5}	5.67	9.51×10^{-7}	5.25
WENO-HLLC	25	2.14×10^{-2}		9.68×10^{-4}	
	50	3.39×10^{-4}	5.98	1.55×10^{-5}	5.96
	100	1.31×10^{-5}	4.70	9.03×10^{-7}	4.10
WENO-MUSTA	25	1.84×10^{-2}		1.35×10^{-3}	
	50	2.30×10^{-4}	6.32	1.26×10^{-5}	6.74
	100	1.29×10^{-5}	4.16	8.99×10^{-7}	3.81
WENO schemes with piece-wise quintic ($r = 6$) reconstruction.					
WENO-FORCE	25	3.34×10^{-2}		9.48×10^{-4}	
	50	4.94×10^{-4}	6.08	1.88×10^{-5}	5.66
	100	1.29×10^{-5}	5.26	8.90×10^{-7}	4.40
WENO-HLLC	25	2.04×10^{-2}		6.41×10^{-4}	
	50	1.87×10^{-4}	6.77	9.87×10^{-6}	6.02
	100	1.27×10^{-5}	3.88	8.92×10^{-7}	3.47
WENO-MUSTA	25	1.63×10^{-2}		6.91×10^{-4}	
	50	1.66×10^{-4}	6.62	8.71×10^{-6}	6.31
	100	1.27×10^{-5}	3.71	8.92×10^{-7}	3.29

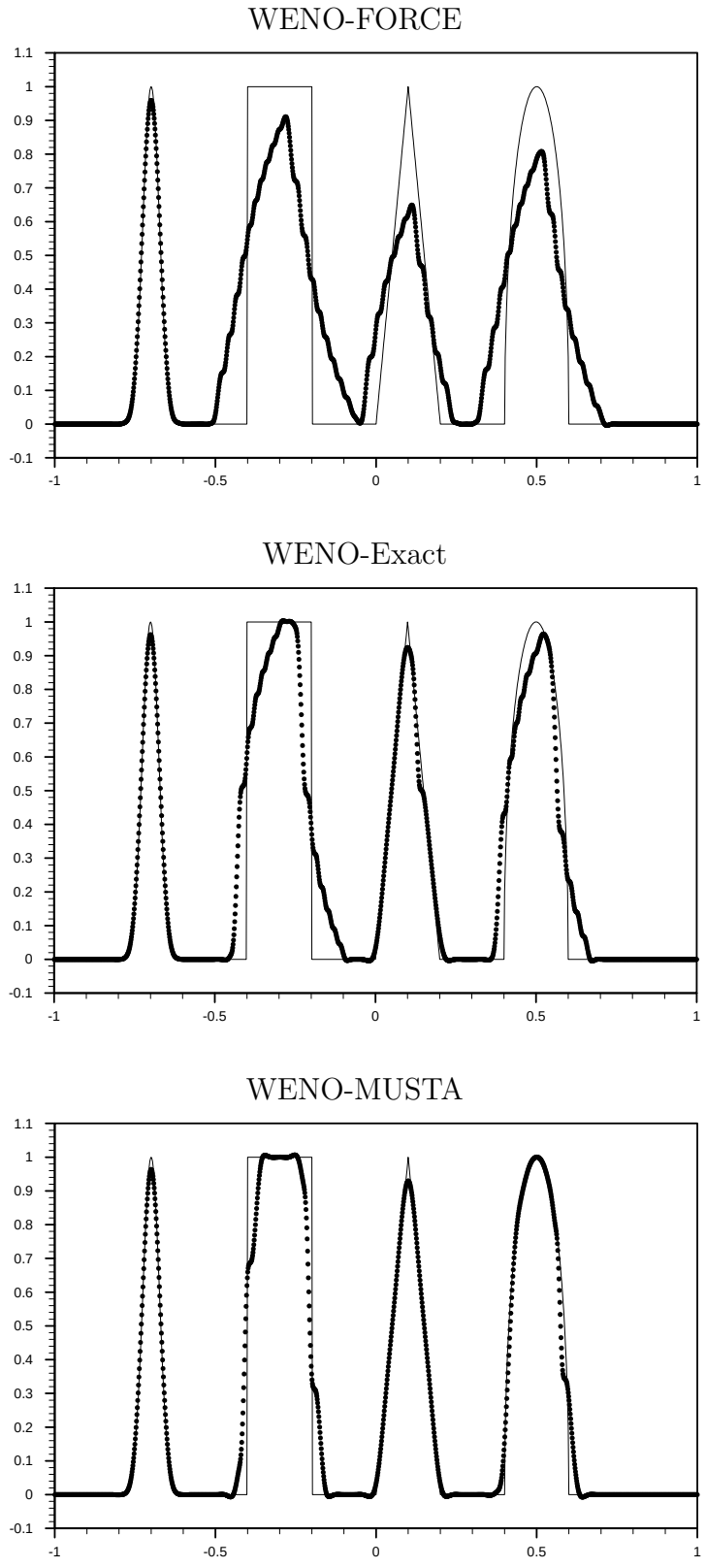

Figure 1: Computed (symbol) and exact (line) solutions for the linear advection equation (50) with initial condition (51) at output time $t = 1000$. Methods used: WENO schemes with piece-wise parabolic reconstruction. $C_{cfl} = 0.4$ and N=1600 cells are used for all schemes.

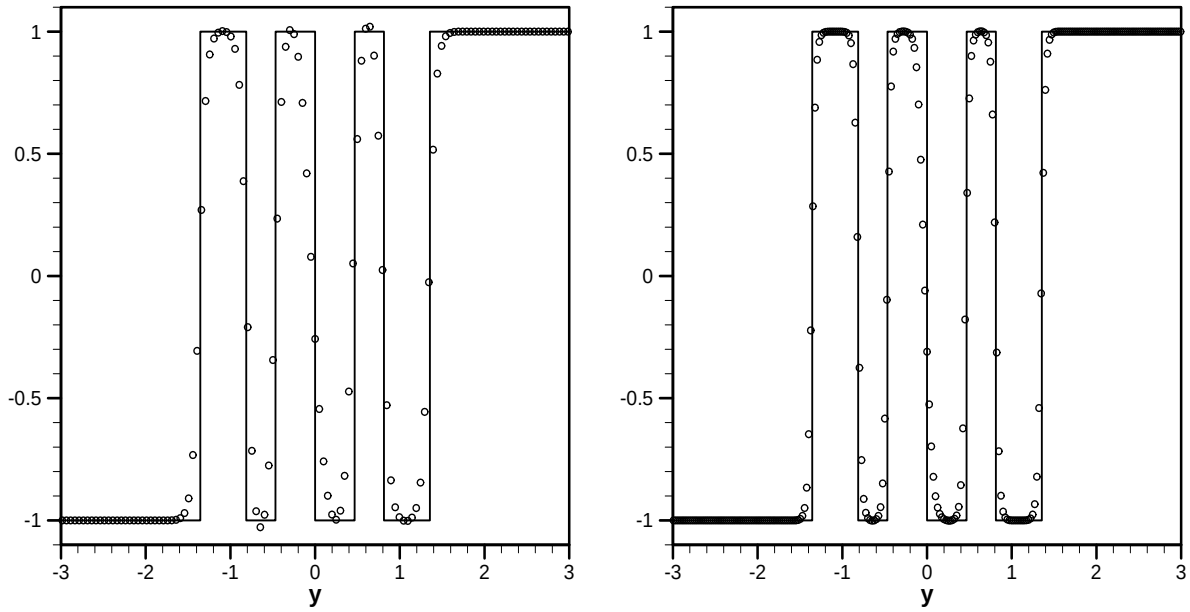

Figure 2: One-dimensional cut along the y axis for the two-dimensional linear advection equation (52) with the initial condition (54) at the output time $t = 4$. $C_{cfl} = 0.45$ is used. The solid line corresponds point-wise values of the exact solution, symbols denote cell averages computed by the WENO-FORCE scheme. The meshes of 201×201 cells (left) and 401×401 cells (right) are used.

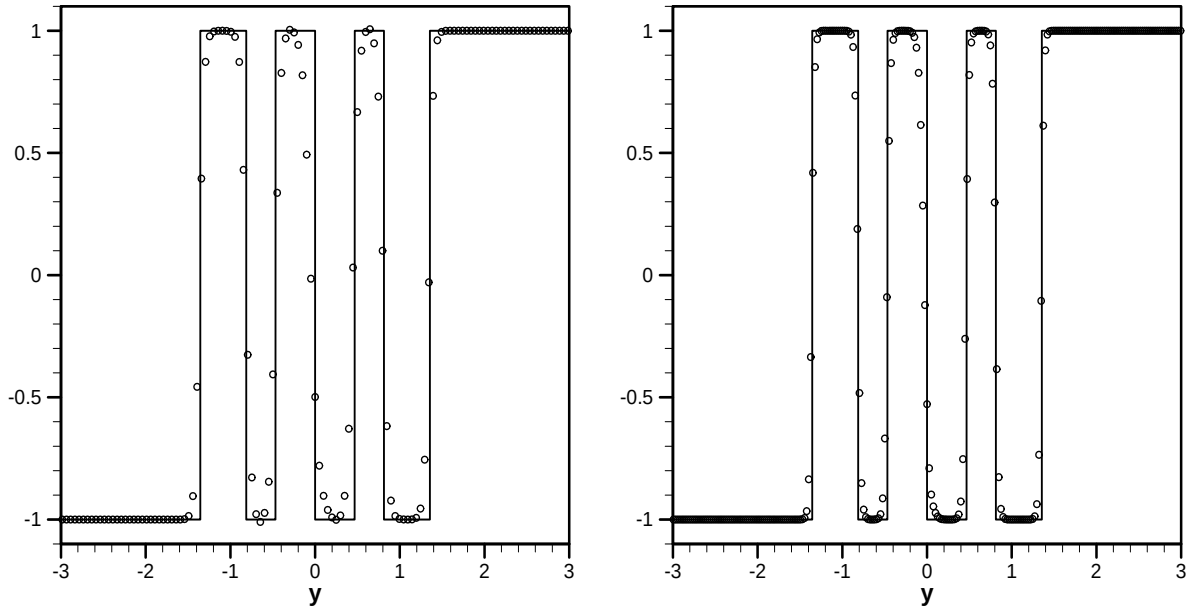

Figure 3: One-dimensional cut along the y axis for the two-dimensional linear advection equation (52) with the initial condition (54) at the output time $t = 4$. $C_{cfl} = 0.45$ is used. The solid line corresponds point-wise values of the exact solution, symbols denote cell averages computed by the WENO-Exact scheme with piece-wise parabolic reconstruction. The meshes of 201×201 cells (left) and 401×401 cells (right) are used.

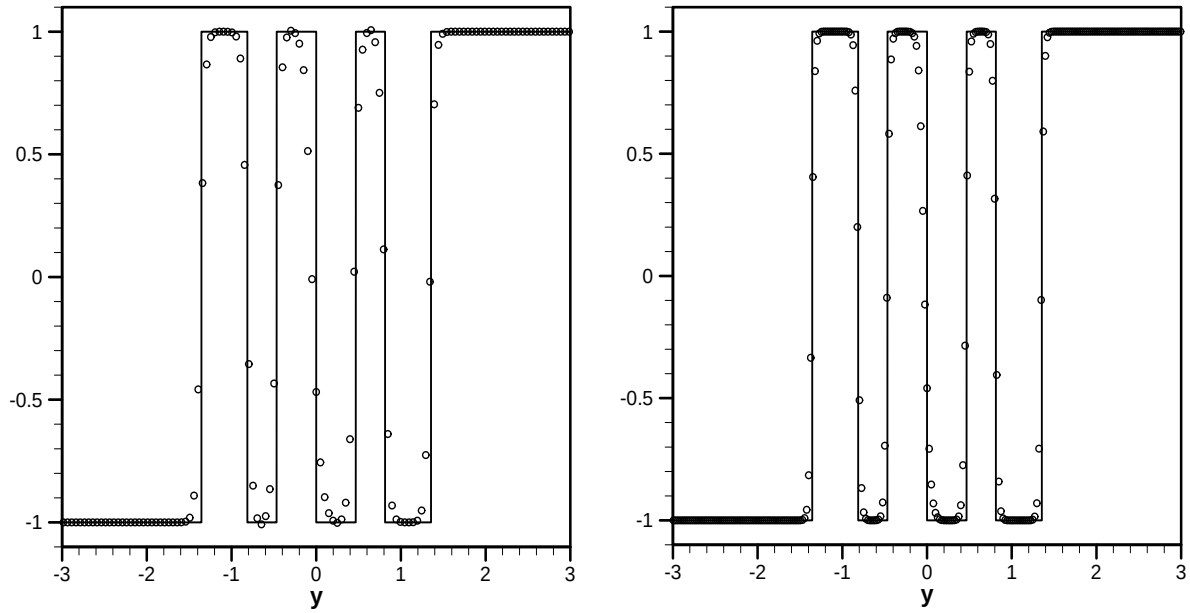

Figure 4: One-dimensional cut along the y axis for the two-dimensional linear advection equation (52) with the initial condition (54) at the output time $t = 4$. $C_{cfl} = 0.45$ is used. The solid line corresponds point-wise values of the exact solution, symbols denote cell averages computed by the WENO-MUSTA scheme with piece-wise parabolic reconstruction. The meshes of 201×201 cells (left) and 401×401 cells (right) are used.

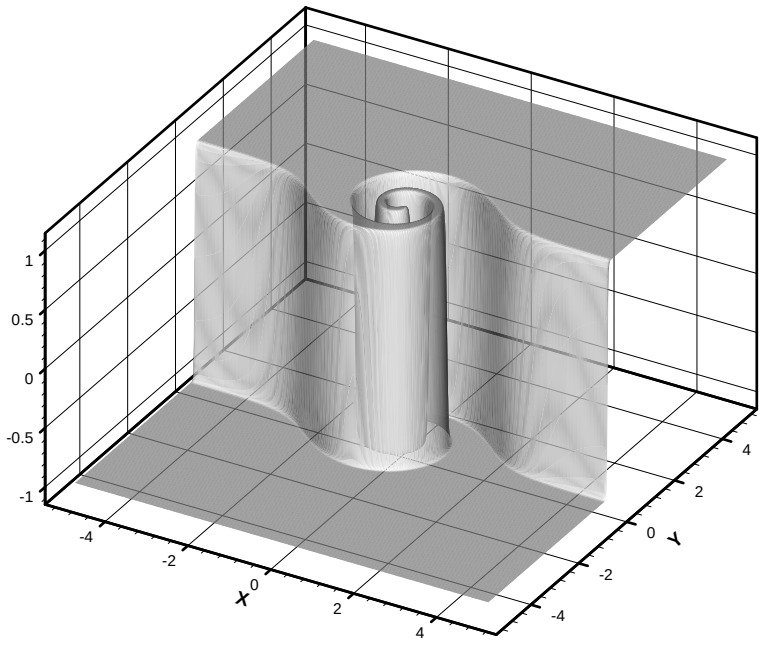

Figure 5: Solution of the two-dimensional linear advection equation (52) with the initial condition (54) at the output time $t = 4$. $C_{cfl} = 0.45$ is used. Method: the WENO-MUSTA scheme with piece-wise parabolic reconstruction. The mesh of 401×401 cells is used.

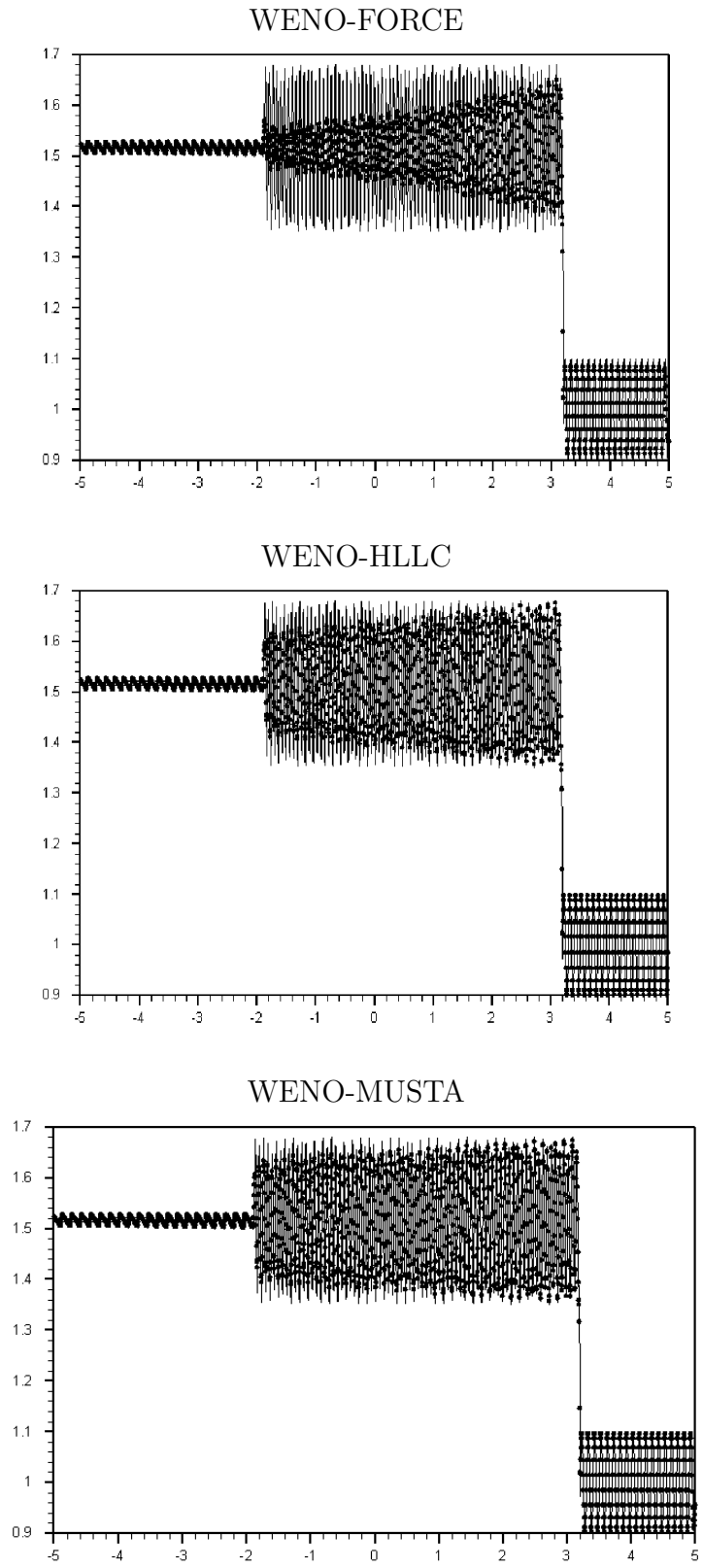

Figure 6: Computed (symbol) and reference (line) solutions for the Euler equations (43) with initial condition (58) at output time $t = 5$. Methods used: WENO schemes with FORCE, HLLC and MUSTA fluxes. $C_{cfl} = 0.6$ and N=2000 cells are used for all schemes.

Density Internal energy

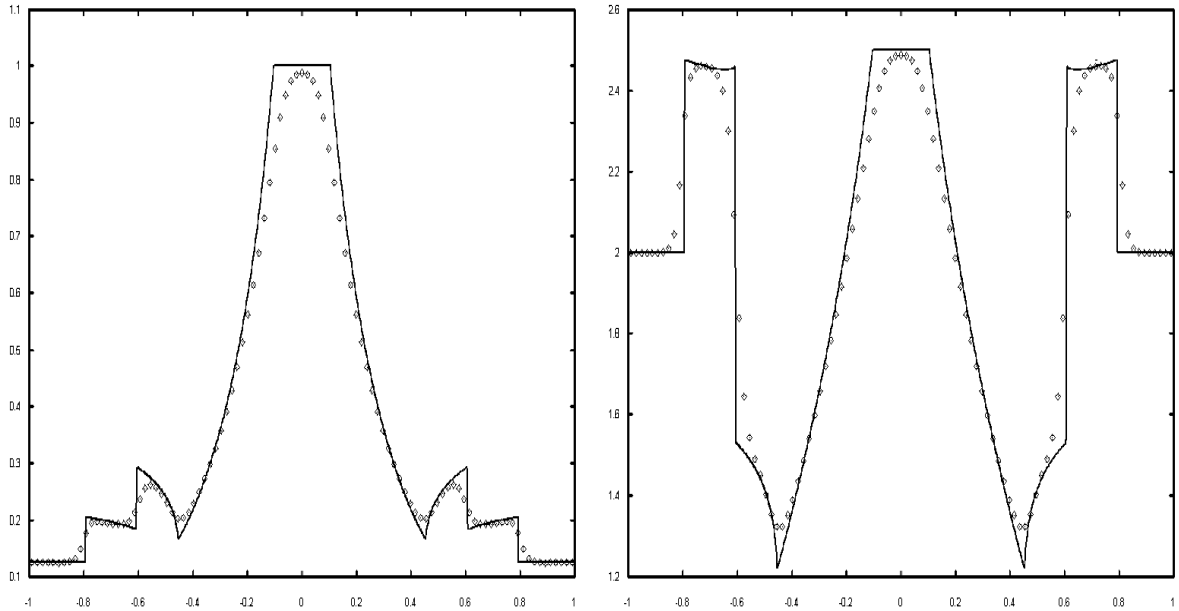

Figure 7: Spherical explosion test problem for the three-dimensional Euler equations. Method used: WENO-FORCE with piece-wise parabolic ($r = 3$) reconstruction, $C_{cfl} = 0.27$ and the mesh of $N = 101$ cells in each coordinate direction.

Density Internal energy

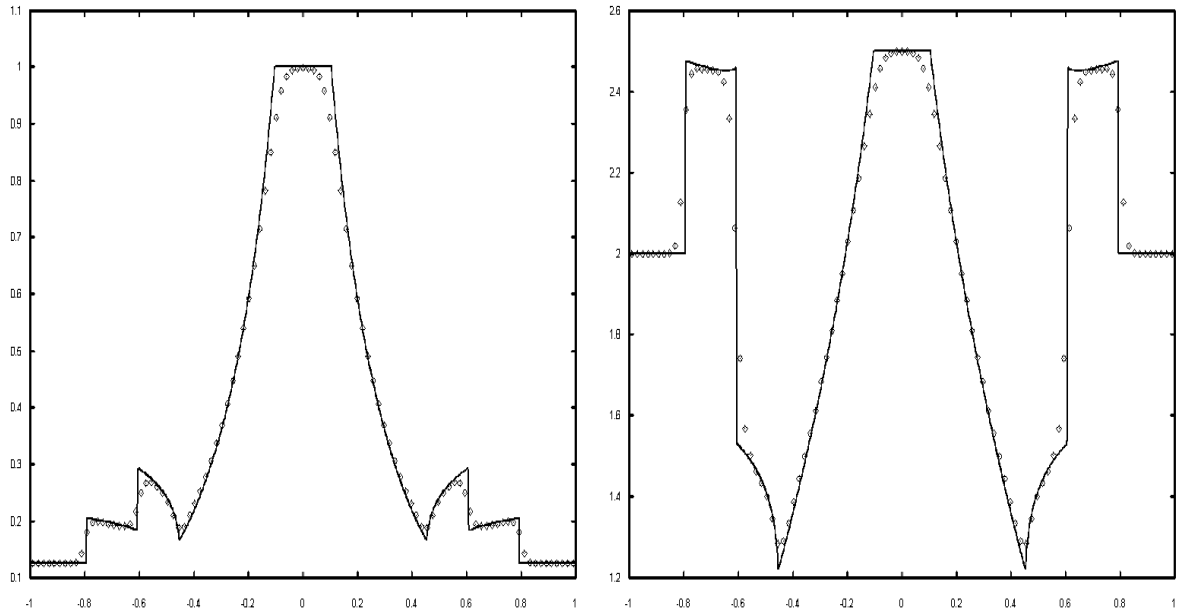

Figure 8: Spherical explosion test problem for the three-dimensional Euler equations. Method used: WENO-HLLC with piece-wise parabolic ($r = 3$) reconstruction, $C_{cfl} = 0.27$ and the mesh of $N = 101$ cells in each coordinate direction.

Density Internal energy

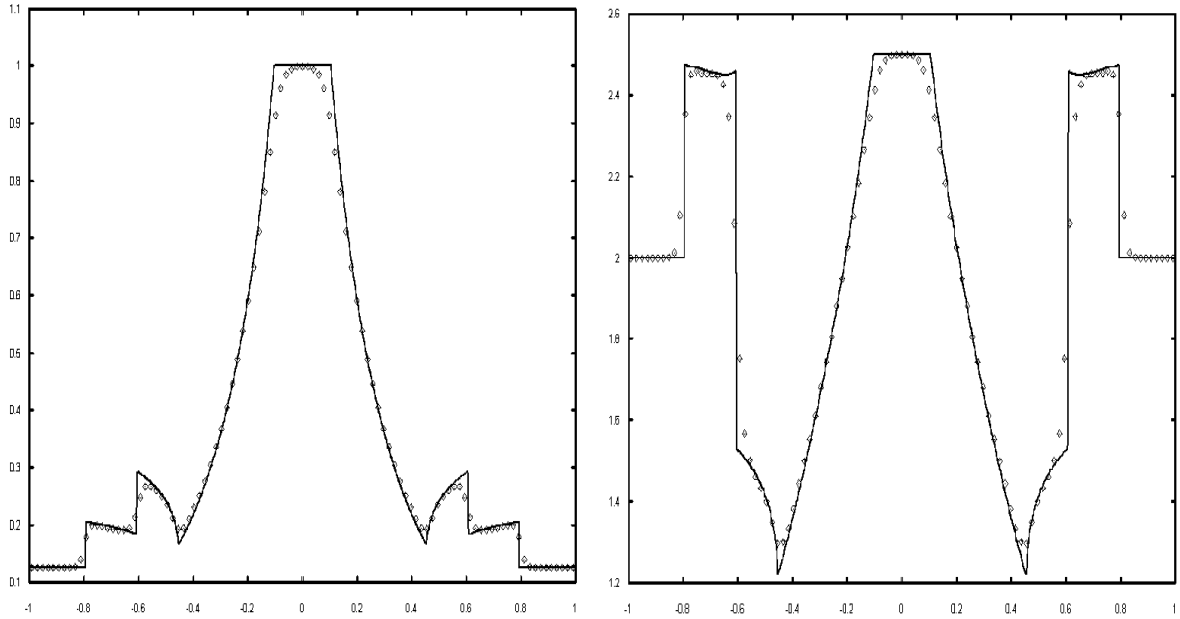

Figure 9: Spherical explosion test problem for the three-dimensional Euler equations. Method used: WENO-MUSTA with piece-wise parabolic reconstruction, $C_{cfl} = 0.27$ and the mesh of $N = 101$ cells in each coordinate direction.

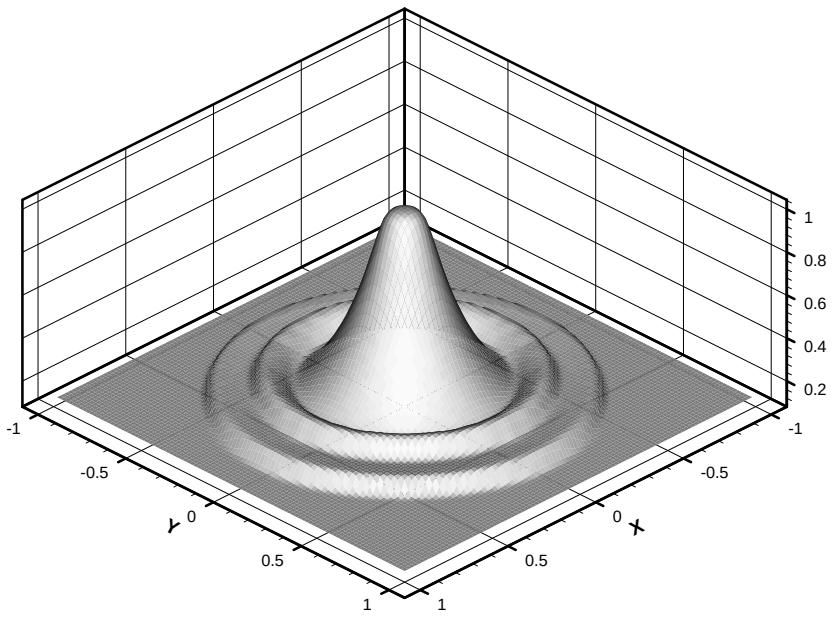

Figure 10: The spherical explosion test problem for the three-dimensional Euler equations. Method used: WENO-MUSTA with piece-wise parabolic ($r = 3$) reconstruction, $C_{cfl} = 0.27$ and the mesh of $N = 101$ cells in each coordinate direction. Density distribution on plane $z = 0$ at time $t = 0.25$

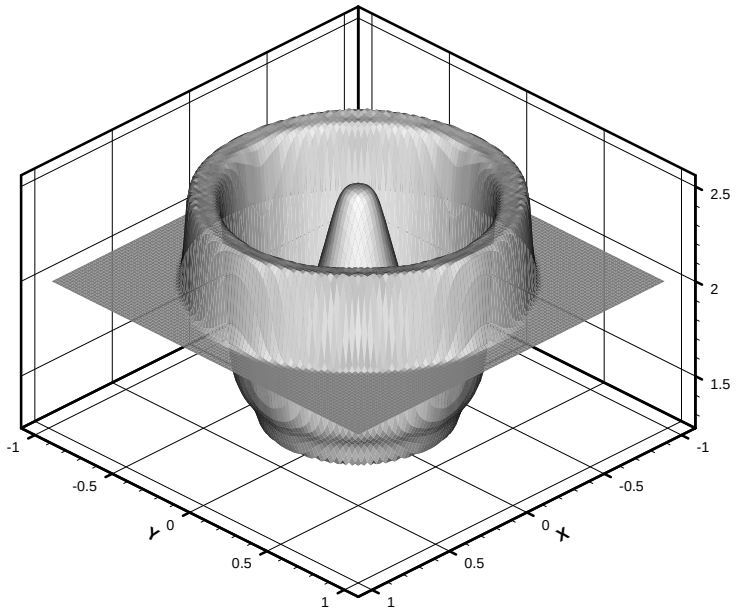

Figure 11: The spherical explosion test problem for the three-dimensional Euler equations. Method used: WENO-MUSTA with piece-wise parabolic ($r = 3$) reconstruction, $C_{cfl} = 0.27$ and the mesh of $N = 101$ cells in each coordinate direction. Internal energy distribution on plane $z = 0$ at time $t = 0.25$